BMC Biology

RESEARCH ARTICLE

Open Access

Foxg1 regulates translation of neocortical neuronal genes, including the main NMDA receptor subunit gene, *Grin1*

Osvaldo Artimagnella[1,3†], Elena Sabina Maftei[1†], Mauro Esposito[2,4], Remo Sanges[2] and Antonello Mallamaci[1*]

Abstract

Background Mainly known as a transcription factor patterning the rostral brain and governing its histogenesis, FOXG1 has been also detected outside the nucleus; however, biological meaning of that has been only partially clarified.

Results Prompted by FOXG1 expression in cytoplasm of pallial neurons, we investigated its implication in translational control. We documented the impact of FOXG1 on ribosomal recruitment of *Grin1*-mRNA, encoding for the main subunit of NMDA receptor. Next, we showed that FOXG1 increases GRIN1 protein level by enhancing the translation of its mRNA, while not increasing its stability. Molecular mechanisms underlying this activity included FOXG1 interaction with EIF4E and, possibly, *Grin1*-mRNA. Besides, we found that, within murine neocortical cultures, de novo synthesis of GRIN1 undergoes a prominent and reversible, homeostatic regulation and FOXG1 is instrumental to that. Finally, by integrated analysis of multiple omic data, we inferred that FOXG1 is implicated in translational control of *hundreds* of neuronal genes, modulating ribosome engagement and progression. In a few selected cases, we experimentally verified such inference.

Conclusions These findings point to FOXG1 as a key effector, potentially crucial to multi-scale temporal tuning of neocortical pyramid activity, an issue with profound physiological and neuropathological implications.

Keywords Foxg1, Translation, Grin1, NMDAR, Neuronal activity

Background

FOXG1 is an evolutionarily ancient transcription factor mastering a number of developmental processes that take place in the rostral brain. These include early activation of pan-telencephalic [1], subpallial [2], and paleo-neopallial [3] programs, promotion of neural precursors self-renewal [4], balance between neuronogenesis and gliogenesis [5–8], and laminar specification of neocortical neurons [9–13]. Later, it promotes morphological maturation of glutamatergic [5, 14, 15] and gabaergic [16] telencephalic neurons. Moreover, FOXG1 sustains activity and excitability of these neurons [7, 16, 17], exerting a complex impact on the transcription of specific gene-sets [17, 18]. Besides, its expression is in turn stimulated by neuronal activity [17, 19]. Finally, FOXG1 promotes hippocampal plasticity, by enhancing NMDA receptor-mediated currents [15]. As a result of such a pleiotropic impact on brain development and neuronal function, *Foxg1* mutations result in complex, cognitive,

†Osvaldo Artimagnella and Elena Sabina Maftei contributed equally to this work.

*Correspondence:
Antonello Mallamaci
amallama@sissa.it
[1] Laboratory of Cerebral Cortex Development, SISSA, Via Bonomea 265, 34136 Trieste, Italy
[2] Laboratory of Computational Genomics, SISSA, via Bonomea 265, 34136 Trieste, Italy
[3] Present Address: IRCCS Centro Neurolesi "Bonino-Pulejo", Messina, Italy
[4] Present Address: Neomatrix SRL, Rome, Italy

and behavioral phenotypes, in both mutant mouse models and human patients. In the mouse, loss of *Foxg1* leads to defective social interaction and impaired spatial learning and memory [15, 20]. Moreover, a co-misregulation of *Foxg1* in postnatal excitatory as well as inhibitory neurons is necessary and sufficient to evoke the emergence of ASD-like phenotypes [21]. In humans, > 120 distinct *FOXG1* mutations result into a complex series of neuropathologies, collectively referred to as *FOXG1* syndrome, including brain dismorphologies, epilepsy, and ASD-like symptoms [22–29]. Moreover, a specific *FOXG1* upregulation has been detected in brain organoids originating from ASD-patient iPSCs [30].

Albeit mainly known as a transcription factor [31], FOXG1 was also previously reported to be in the *cytoplasm* of olfactory placode and early born neocortical neurons [32], as well as in the cytoplasm and mitochondria of a hippocampal neuronal line and whole brain homogenates [33]. Next, three high throughput screenings in HEK293T, yeast, and N2A cells [34–36] showed that FOXG1 may interact with a number of factors implicated in post-transcriptional gene regulation, including translation. In addition, we noticed that murine FOXG1 harbors a YATHHLT motif (at 366–372 position), conserved among vertebrates and reminiscent of the EIF4E-binding motif detectable in EIF4E-BP, eIF4G, and other effectors [37]. These observations suggest a possible involvement of FOXG1 in the control of mRNA translation.

To address this issue, we interrogated primary neocortical cultures via a variety of complementary experimental approaches. We found that—in neuronal soma as well as in neurites—FOXG1 promotes translation of *Grin1*, encoding for the main subunit of the NMDA receptor and playing a pivotal role in neuronal plasticity. Interestingly, this requires FOXG1 interaction with EIF4E. We also demonstrated that FOXG1 promotes fast homeostatic tuning of GRIN1, an issue of potential relevance to the etiopathogenesis of *FOXG1*-linked neurological disorders. Finally, we got evidence that FOXG1 modulates ribosomal recruitment of dozens of other mRNAs encoding for effectors of neuronal activity, and it also affects ribosome progression. In this way, beyond their "slow" and cell-wide impact on gene expression, originating from transcription regulation, fluctuations of FOXG1 levels might be implicated in a far more complex control on neuronal functions, at different timescales, and in distinctive regions of cell cytoplasm.

Results

Subcellular FOXG1 localization in pallial neurons

To corroborate previous reports about non-nuclear FOXG1 localization, first, we profiled murine, E16.5 + DIV8 neocortical neurons (Fig. 1A) for subcellular distribution of anti-FOXG1 immunoreactivity. In addition to the nucleus, we found FOXG1 in TUBB3^{+} soma and neurites (Fig. 1A, a,b), as well as—more specifically—in punctate-PSD95^{+} dendrites (Fig. 1A, c,d) and SMI312^{+} axons (Fig. 1A, d,e). Then, to get further information about partition of non-nuclear FOXG1 between mitochondria and cytosol, we transduced murine P0 + DIV3 hippocampal precursors by a TetON-controlled transgene encoding for a FOXG1-EGFP chimera, we activated it at DIV5, and, upon pre-terminal mitochondria staining by MitoTracker, at DIV8, we profiled living neurons for fluorescence distribution by confocal microscopy and Volocity analysis (Fig. 1B). For simplicity, we restricted the analysis to mid-distal neurites. Specifically, we quantified (1) the MitoTracker^{ON} and MitoTracker^{OFF} fractions of the EGFP^{ON} space, (2) the average intensity of EGFP signal peculiar to each Mitotracker$^{ON/OFF}$ fraction, and (3) the cumulative EGFP signal ending in each fraction. We found that mitochondria occupied almost 30% of neurite volume

(See figure on next page.)

Fig. 1 Neuronal, subcellular FOXG1 localization. **A** Preparations obtained by dissociation of E16.5 murine neocortices were cultured up to day in vitro 8 (DIV8), under pro-differentiative medium supplemented with AraC. They were co-immunoprofiled for FOXG1 and, alternatively, pan-neuronal TUBB3 (a,b), dendritic PSD95 (c,d), and axonal SMI312 (d,f) antigens, by confocal microscopy. High power magnifications (3x, 3x, and 4x) of (a,c,e) panel insets are in (b,d,f), respectively. Arrowheads point to FOXG1-immunoreactive grains adjacent to TUBB3-positive bundles (b), PSD95-positive spots (d), and SMI312-positive bundles (f). Scalebars, 20 µm. **B** Preparations obtained by dissociation of P1 murine hippocampi were engineered to overexpress a FOXG1-EGFP chimera and profiled at DIV8 for cytoplasmic-vs-mitochondrial EGFP partition. As detailed in the protocol to the left, cultures were set in pro-differentiative medium, transduced at DIV3 by lentiviral vectors driving p(Pgk1)/Tet^{ON}-controlled FOXG1-EGFP chimera expression, supplemented at DIV5 by 2 µg/ml doxycyclin, preterminally labeled by 50 nM MitoTracker dye for 30 min, and finally profiled for EGFP partition between mitochondria and cytosol, by live confocal microscopy and Volocity-analysis. Profiling was limited to intermediate/distal neuritic segments, where three parameters were evaluated: (1) the cytoplasmic (Mitotracker^{OFF}) and mitochondrial (Mitotracker^{ON}) fractions of the EGFP^{ON} volume, (2) the average EGFP intensity in cytoplasmic and mitochondrial compartments, and (3) the cumulative fraction of EGFP signal falling in these two compartments. *n* is the number of neurons profiled, evenly collected from three biological replicates (i.e., independently cultured and engineered aliquots originating from the same starting pool of neural cells). **C** Examples of FOXG1-EGFP/Mitotracker distribution in intermediate (a) and distal (c) dendritic segments. High power magnifications of (a,c) panel insets are in (b,d), respectively. Scalebars, 20 µm. Arrowheads in (b,d) point to cytoplasmic FOXG1-EGFP signal in an intermediate dendrite segment and lamellipodia/filopodia, respectively

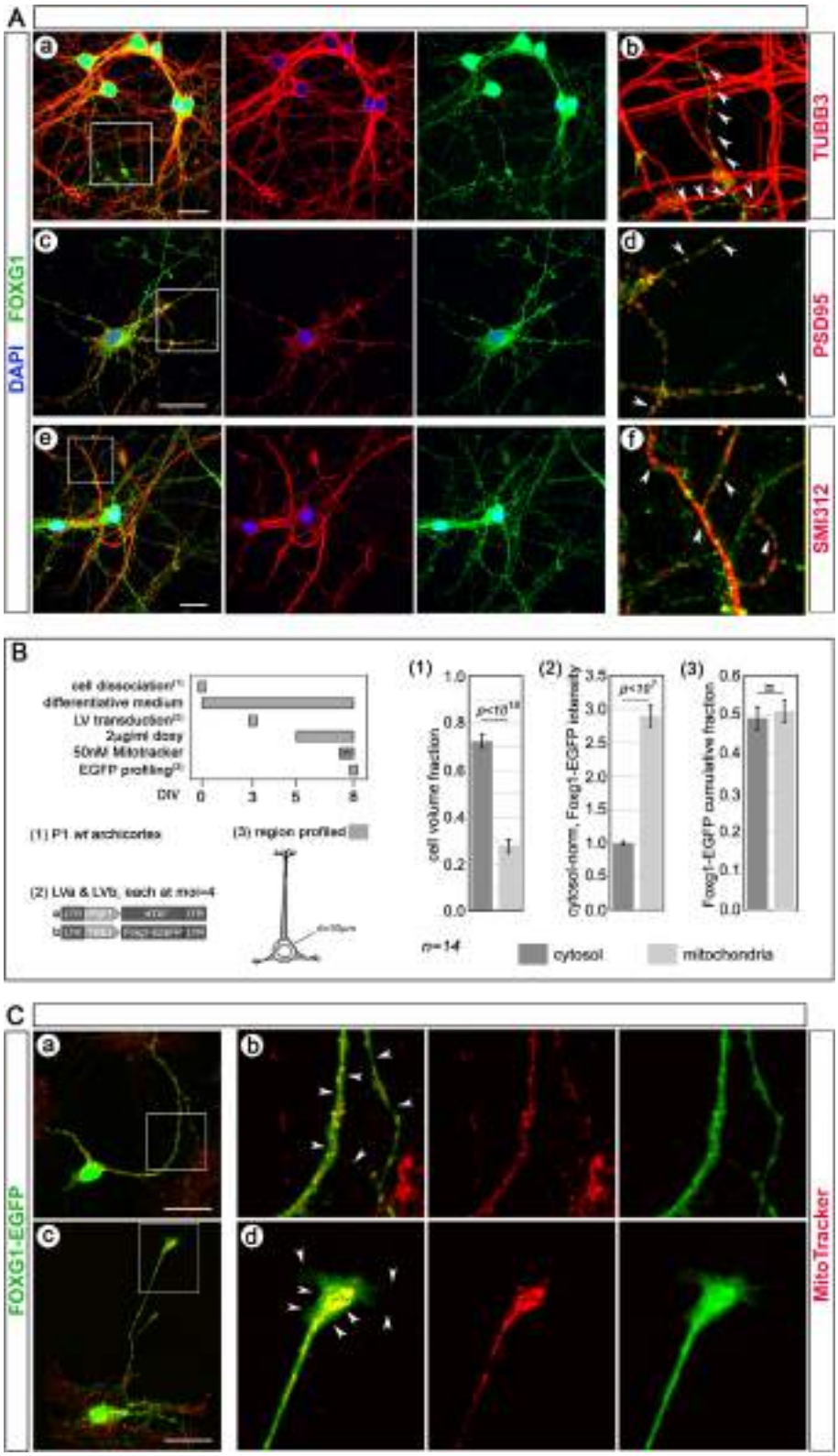

Fig. 1 (See legend on previous page.)

and that EGFP density was almost three times higher in mitochondria than in cytoplasm. That resulted in a substantial, cumulative equipartition of the FOXG1-EGFP chimera between the former and the latter. Intriguingly, large patches of non-mitochondrial EGFP could be specifically detected at distal ends of neuritic processes, including lamellipodia and filopodia (Fig. 1C).

FOXG1 promotes *Grin1*-mRNA translation in neocortical neurons

To explore FOXG1 implication in translation, we selected a small sample of genes undergoing translational regulation and/or being implicated in fine-tuning of neuronal activity (*Grid1*, *Grin1, Slc17a6*, *Gria1*, *Gabra1*, *Bdnf -2c* and *4* isoforms -, *Psd95*, and *Foxg1)* [38, 39], and we evaluated the impact of *Foxg1* expression level on ribosomal engagement of their mRNAs. For this purpose, we used neocortical neurons obtained from E16.5 $Rpl10a^{E\text{-}GFP-Rpl10a/+}$ mouse embryos [40] we engineered to conditionally overexpress *Foxg1* (*Foxg1*-OE) or a *PLAP* control (Additional file 1: Figure S1). Four days after transgenes activation, at DIV8, we analyzed them by translating ribosome affinity purification (TRAP)-qRTPCR (Fig. 2A, to left). Specifically, by means of an anti-EGFP antibody, we purified RNA associated to EGFP-tagged ribosomes (IP component) and supernatant RNA (SN component). Then, we scored these RNAs by qRT-PCR, for transcripts originating from the abovementioned candidate genes. Upon normalization of IP and SN values against *Rpl10a*-mRNA, IP/SN ratios peculiar to *Foxg1*-OE samples were averaged and further normalized against *PLAP* controls. *Grid1* and *Grin1* IP/SN ratios were upregulated in *Foxg1*-OE samples (+50.7 ± 16.2%, with $p < 0.02$ and $n = 6,6$; and +34.7 ± 7.0%, with $p < 0.02$ and $n = 6,6$, respectively), suggesting that FOXG1 may promote ribosomal engagement of their mRNAs. The IP/SN index was not affected in case of other genes subject of investigation (Fig. 2B).

To corroborate this finding and explore its biological meaning, we focused our attention on *Grin1* gene, encoding for the main subunit of NMDA receptor, whose activity is impaired upon conditional *Foxg1* ablation in the murine hippocampus [15]. For this gene, we evaluated the protein-to-mRNA ratio upon artificial modulation of *Foxg1* expression. Tests were run in cultures of E16.5 + DIV8 murine neocortical neurons, engineered to conditionally overexpress *Foxg1* (Additional file 1: Figure S1; Fig. 2A, to left) or reduce its level (*Foxg1*-LOF) (Additional file 1: Figure S1; Fig. 2A, to right). GRIN1 protein was quantified via WB, by a monoclonal antibody recognizing an epitope encoded by *Grin1*-exon 20. *Grin1*-mRNA was measured via qRTPCR, by two oligonucleotide pairs, detecting all *Grin1* isoforms (*pan-Grin1*) or exon20-containing ones (*ex20-Grin1*) (Fig. 2C). Normalized against betaACTIN, GRIN1 protein was decreased by 36.7 ± 4.7% (with $p < 0.01$ and $n = 4,4$) and increased by 12.8 ± 3.8% (with $p < 0.02$ and $n = 4,4$), following down- (Fig. 2D) and upregulation (Fig. 2E) of *Foxg1*, respectively. Opposite trends were displayed by *pan-Grin1*-mRNA (+6.9 ± 2.0%, with $p < 0.04$ and $n = 4,4$, in *Foxg1*-LOF samples; −13.7 ± 4.7%, with $p < 0.04$ and $n = 4,4$, in *Foxg1*-OE ones). Remarkably, such trends were even more pronounced in the case of *ex20-Grin1*-mRNA (+31.5 ± 13.0%, with $p < 0.07$ and $n = 4,4$, in *Foxg1*-LOF samples; −17.7 ± 7.0%, with $p < 0.05$ and $n = 4,4$ in *Foxg1*-OE ones) (Fig. 2D, E). Finally, to get a comprehensive index of the post-transcriptional impact exerted by *Foxg1* on *Grin1* expression, we calculated the "GRIN1-protein/*Grin1*-mRNA" ratios peculiar to *Foxg1*-misexpressing cultures and normalized them against their controls. Such ratios ranged from 0.59 (*Foxg1*-LOF) to 1.31 (*Foxg1*-OE), referring to *pan-Grin1*-mRNA, and from 0.48 (*Foxg1*-LOF) to 1.37 (*Foxg1*-OE), referring to *ex20-Grin1*-mRNA (Fig. 2F). All suggests that *Foxg1* plays a robust positive impact on post-transcriptional tuning of GRIN1-protein levels.

Next question was (1) does *Foxg1* enhance the translation of *Grin1*-mRNA and/or (2) does it diminish the degradation of GRIN1 protein?

As for (1), we assessed Grin1 translation rates in E16.5 + DIV8 neocortical cultures made *Foxg1*-LOF by RNAi (Additional file 1: Figure S1). To this aim, we terminally pulsed these cultures with puromycin and we measured levels of nascent GRIN1 protein, (n)GRIN1, via anti-GRIN1/anti-puromycin-driven proximity ligation assay (PLA) (Fig. 3A). To distinguish among translation of all *Grin1*-mRNA isoforms (*pan-Grin1*) and exon20-containing ones (*ex20-Grin1*), two anti-GRIN1 antibodies were alternatively used in addition to anti-puromycin (Fig. 3A, a and b). The former, anti-GRIN1-NH2-term, recognizes the amino-terminal protein region shared by all isoforms (hereafter collectively referred to as "pan-GRIN1"). The latter, anti-GRIN1-COOH-term, interacts with a more carboxyterminal ex20-encoded epitope, restricted to a smaller isoform set (hereafter collectively referred as "ex20-GRIN") (Fig. 2C). Moreover, the analysis was firstly run on whole neurons and then limited to neurites. In case of whole neurons, two indices of (n) GRIN1 levels were evaluated, the cumulative PLA signal per cell and the cumulative PLA signal per spot. In case of neurites, the first parameter was hard to evaluate, and the measure was restricted to the cumulative PLA signal per spot. Compared to controls, whole neuron (n) pan-GRIN1 signal was reduced in *Foxg1*-LOF samples, by 6.7 ± 1.8% per cell ($p < 0.039$, $n = 7,8$), and 15.6 ± 2.9% per spot ($p < 0.003$, $n = 7,8$). In a similar way, neurite (n) pan-GRIN1 signal per spot was decreased by 11.0 ± 3.5%

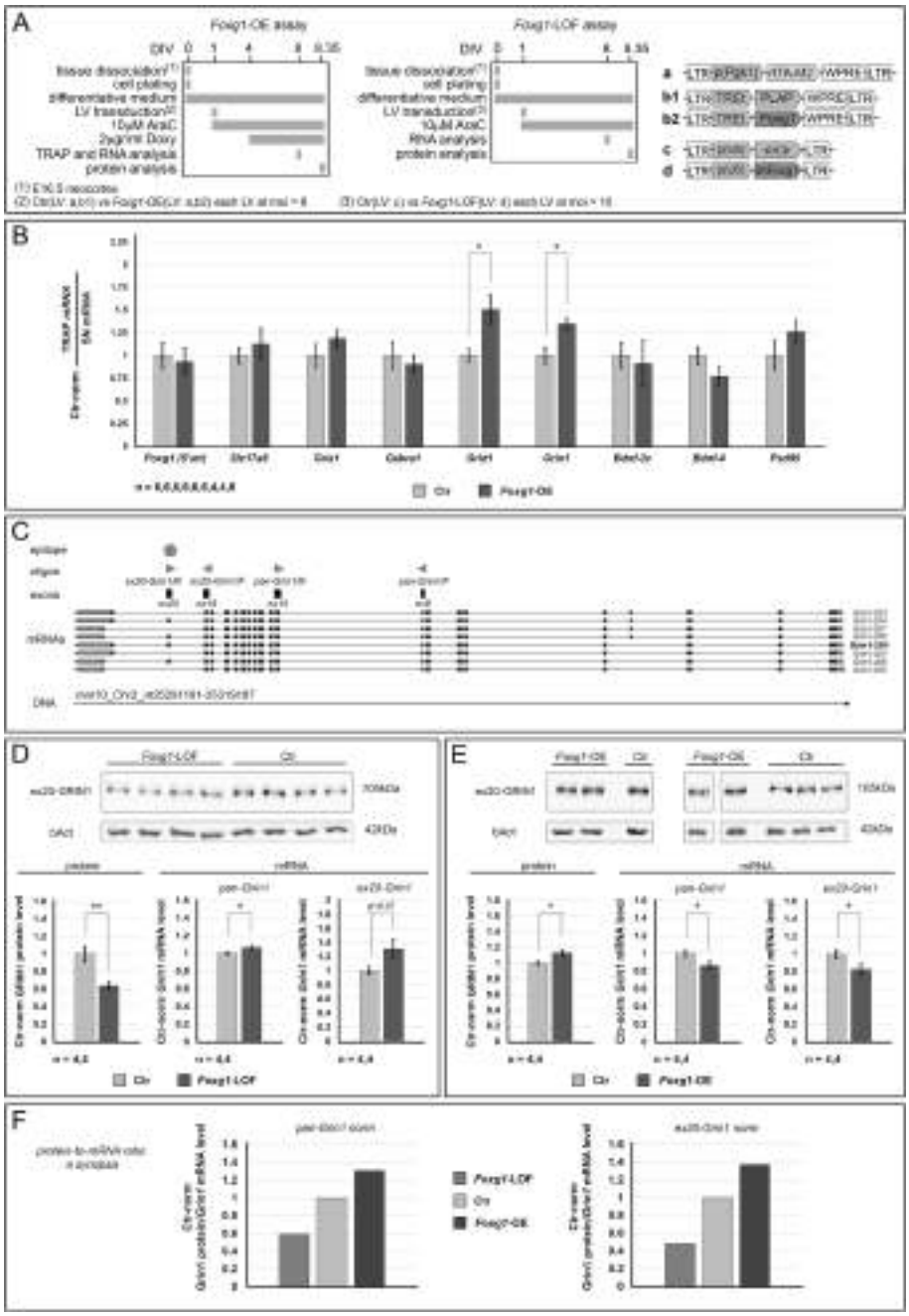

Fig. 2 Impact of *Foxg1* manipulation on ribosomal allocation and protein output of selected neuronal transcripts. **A** Protocols and lentiviral vectors used to engineer neocortical cultures to conditionally overexpress *Foxg1* (Foxg1-OE, left panel) or reduce its level (*Foxg1*-LOF, right panel). **B** Comparative translating ribosome affinity purification (TRAP) quantification of ribosome-associated mRNA fraction (TRAP-mRNA) and its supernatant fraction (SN-mRNA), referring to selected neuronal transcripts, in *Foxg1*-OE cultures. mRNA levels measured by qRT-PCR, and double normalized, against *Rpl10a*-mRNA and controls. **C** *Grin1* gene locus with the main polypeptide-encoding transcripts originating from it. The top polygon represents the protein epitope recognized by the anti-Grin1 antibody used in Western blot assays. Arrowheads indicate oligos used to quantify *Grin1*-mRNA, distinguishing between ex20-containing Grin1 (ex20-*Grin1*) isoforms and pan-*Grin1* isoforms. **D**, **E** Western blot analysis of Grin1 protein and qRT-PCR quantification of pan-*Grin1* and ex20-*Grin1* mRNA isoforms, upon *Foxg1*-LOF (**D**) and *Foxg1*-OE (**E**) manipulations. Protein levels double normalized against bAct and controls, mRNA levels against *Rpl10a*-mRNA and controls. **F** Progression of "normalized Grin1-protein" to "normalized *Grin1*-mRNA" ratio upon *Foxg1* manipulation, referring to pan-*Grin1* mRNA (left graph) or ex20-*Grin1*-mRNA (right graph). Throughout figure, *n* is the number of biological replicates, i.e., independently cultured and engineered preparations, originating from a common neural cell pool. Statistical evaluation of results was performed by *t*-test, two-tailed (**B**, **D**), or one-tailed (**E**), unpaired and homoscedastic. * $p < 0.05$, ** $p < 0.01$. Errors bars indicate s.e.m

($p < 0.043$, $n = 7,8$) (Fig. 3A, a). As for (n)ex20-GRIN1, its signal was also reduced in *Foxg1*-LOF samples, by 20.9 ± 6.1% per cell ($p < 0.013$, $n = 8,8$) and 14.4 ± 3.6% per spot ($p < 0.003$, $n = 8,8$). In a similar way, neurite (n)ex20-GRIN1 signal per spot was also decreased by 7.7 ± 3.2% ($p < 0.048$, $n = 8,8$) (Fig. 3A, b). In a few words, dampening *Foxg1* reduces GRIN1 synthesis, in soma as well as in neurites. Interestingly, this is peculiar to GRIN1, and it does not apply to all translatome, as shown by anti-puro immunofluorescence (IF) run on *Foxg1*-LOF neural cultures terminally treated by emetine and puromycin (Fig. 3B). Taking into account the 6.9% and 31.5% increases undergone by *pan-Grin1-* and *ex20-Grin1*-mRNA, respectively, upon *Foxg1* downregulation (see Fig. 2D), these data suggest that *Foxg1* specifically promotes *Grin1*-mRNA translation, with particular emphasis on its ex20-containing isoforms.

As for (2), we evaluated GRIN1 degradation rates in similar *Foxg1*-LOF neocortical samples. To this aim, we blocked translation by cycloheximide and monitored time course progression of previously synthesized GRIN1 protein over 14 h (Fig. 3C, to left). Remarkably, GRIN1 degradation rate resulted to be not increased, but—rather—it displayed a slight decreasing trend upon *Foxg1* downregulation. Specifically, the GRIN1(ti)/GRIN1(t0) ratio equalled $e^{[-(0.039/h)*t(i)]}$ and $e^{[-(0.067/h)*t(i)]}$ in *Foxg1*-LOF cultures and controls, respectively (with $p < 0.093$, $n = 3,3,3,3,3$) (Fig. 3C, to right). This result rules out that the increase of "GRIN1-protein/*Grin1*-mRNA ratio" evoked by higher *Foxg1* expression (Fig. 2F) may be enhanced by FOXG1 impact on GRIN1 protein degradation.

Finally, concerning the process through which FOXG1 promotes *Grin1*-mRNA translation, we reasoned that the cumulative translation gain peculiar to a given mRNA is a function of both the rate of ribosomes engagement to such mRNA and the speed at which they progress along its cds. We have shown that FOXG1-dependent promotion of GRIN1 translation firstly reflects an improved recruitment of ribosomes to *Grin1*-mRNA (Fig. 2B). We wondered if FOXG1 is also able to stimulate ribosome progression along *Grin1*-cds. To address this issue, we set a dedicated puro-PLA run-off assay (Additional file 1: Figure S3A-C) and implemented it in neocortical neuronal cultures. Specifically, upon blockade of de novo ribosome recruitment to mRNA cap by harringtonine [41, 42], ribosomes were allowed to continue ongoing translations for a time presumptively close to that required for full *Grin1*-mRNA translation. At the end of this time, unfinished GRIN1 polypeptides were labeled by terminal puromycin supplementation and revealed by anti-Grin1/puro-PLA. The PLA signal was subtracted from its $t = 0$ counterpart (evaluated prior to harringtonine treatment), and the resulting difference, normalized against $t = 0$ value, was employed as an index positively correlated to ribosome progression speed along *Grin1*-cds (Additional file 1: Figure S3; Fig. 4A, top). Such run-off assay was performed on *Foxg1*-LOF samples and their "wild type" controls, driving PLA by anti-GRIN1-NH2-term (which recognizes *all* GRIN1 polypeptides). As expected, 11 min after harringtonine supplementation, (n)pan-GRIN1 signal underwent a substantial decline compared to its $t = 0$ value (almost −40%); however, no difference was detected between *Foxg1*-LOF samples and controls (Fig. 4A, bottom). This suggests that no generalized change of *Grin1*-mRNA *translation speed* occurs upon *Foxg1* manipulation.

(See figure on next page.)

Fig. 3 Quantification of nascent Grin1 protein (**A**) and nascent proteome (**B**) and evaluation of Grin1-protein degradation rate (**C**) in *Foxg1*-LOF neurons. **A** To the top, protocols (including lentiviruses employed and operational details of proximity ligation assay (PLA) analysis), to the bottom, results. Graphs represent quantitative confocal immunofluorescence (IF) assessment of nascent Grin1 protein, (n)Grin1, performed upon *Foxg1* down-regulation, terminal (5') puromycin administration, and subsequent anti-Grin1/anti-puromycin-driven PLA. Two anti-Grin1 antibodies were alternatively used, recognizing (a) amino-terminal (anti-Grin1-NH2-term) and (b) carboxyterminal (anti-Grin1-COOH-term) protein regions. Neuron cell silhouettes were identified by direct EGFP fluorescence, driven by the $Mapt^{EGFP}$ transgene. PLA signal was quantified throughout the whole neuron or restricted to neurites. As indices of (n)Grin1 levels, shown are the average cumulative IF signals per cell and the average cumulative IF signals per spot. **B** To the left, protocols (including lentiviruses employed), to the right, results. Graph represents quantitative confocal immunofluorescence (IF) evaluation of nascent total puromycinilated proteins, performed upon *Foxg1* down-regulation, terminal emetine (25') and puromycin (5') supplementation, and final anti-puromycin-driven IF. In both **A** and **B**, results were normalized against controls, error bars indicate s.e.m., and statistical evaluation of results was performed by one-way *t*-test, one-tailed, unpaired, and homoscedastic (*$p < 0.05$; **$p < 0.01$). In both **A** and **B**, included are examples of primary data referred to by the corresponding graphs. Scale bars, 50 µm. **C** To the left, protocols and lentiviruses employed for this analysis, to the right, results. Graph represents progression of Grin1-protein levels at different *ti* times, evaluated by western blot, upon *Foxg1* down-regulation and subsequent 50 µg/ml cycloheximide (CHX) blockade of translation. For each genotype, results double normalized against (ti)bAct protein levels and (*t*0)average values. Superimposed, exponential trendlines and *y*(*t*) functions. Statistical evaluation of results performed by ANCOVA test. Included are examples of primary data referred to by the corresponding graphs. Throughout the figure, *n* is the number of biological replicates, i.e., independently cultured and engineered preparations, originating from a common neural cell pool

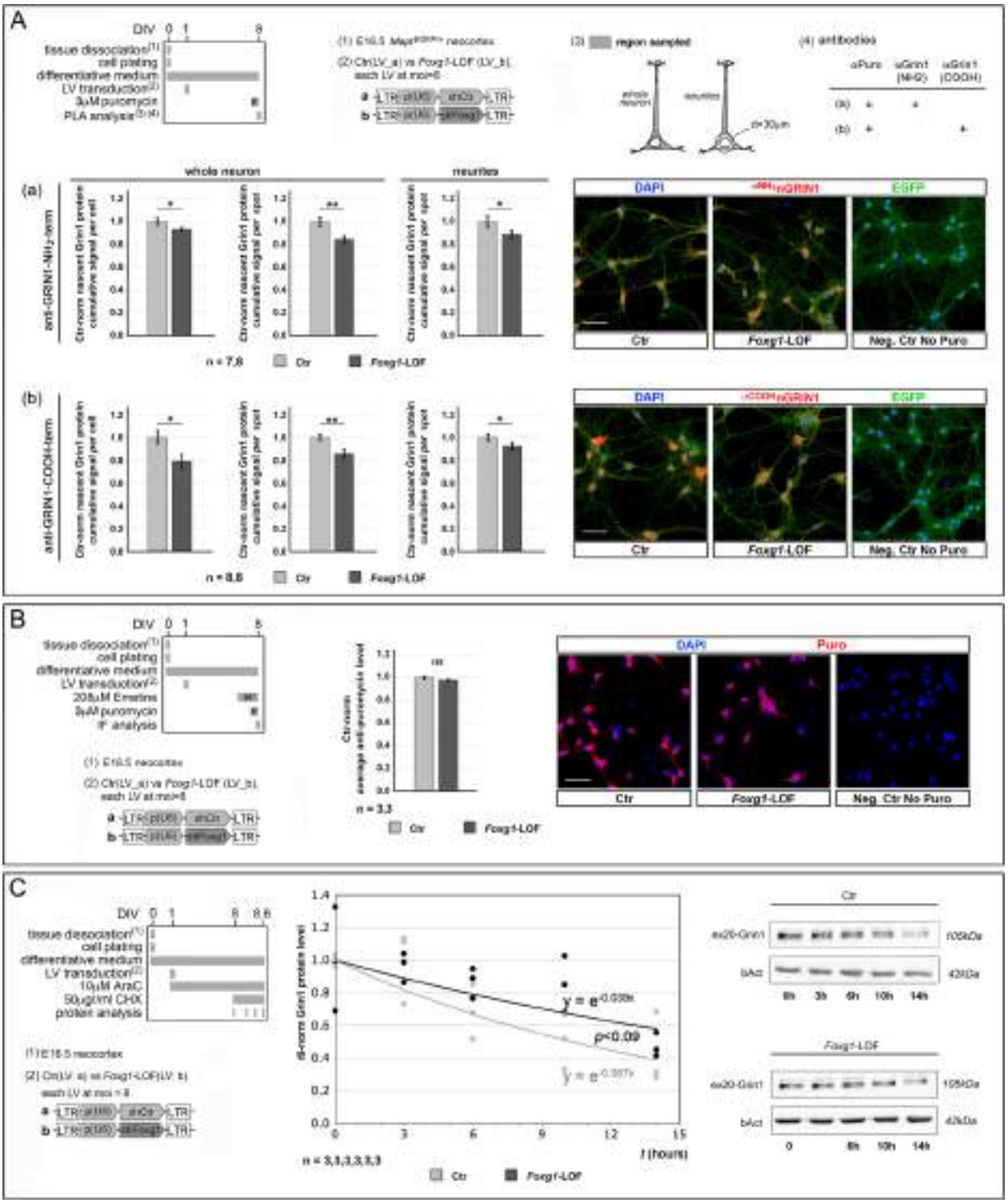

Fig. 3 (See legend on previous page.)

FOXG1 physically interacts with selected translation factors

We have shown that FOXG1 enhances translation of GRIN1. Next question was does FOXG1 stimulate translation (1) acting as a canonical nuclear transcription factor (i.e., tuning transcription of translation factor genes) or (2) working as a proper "translation

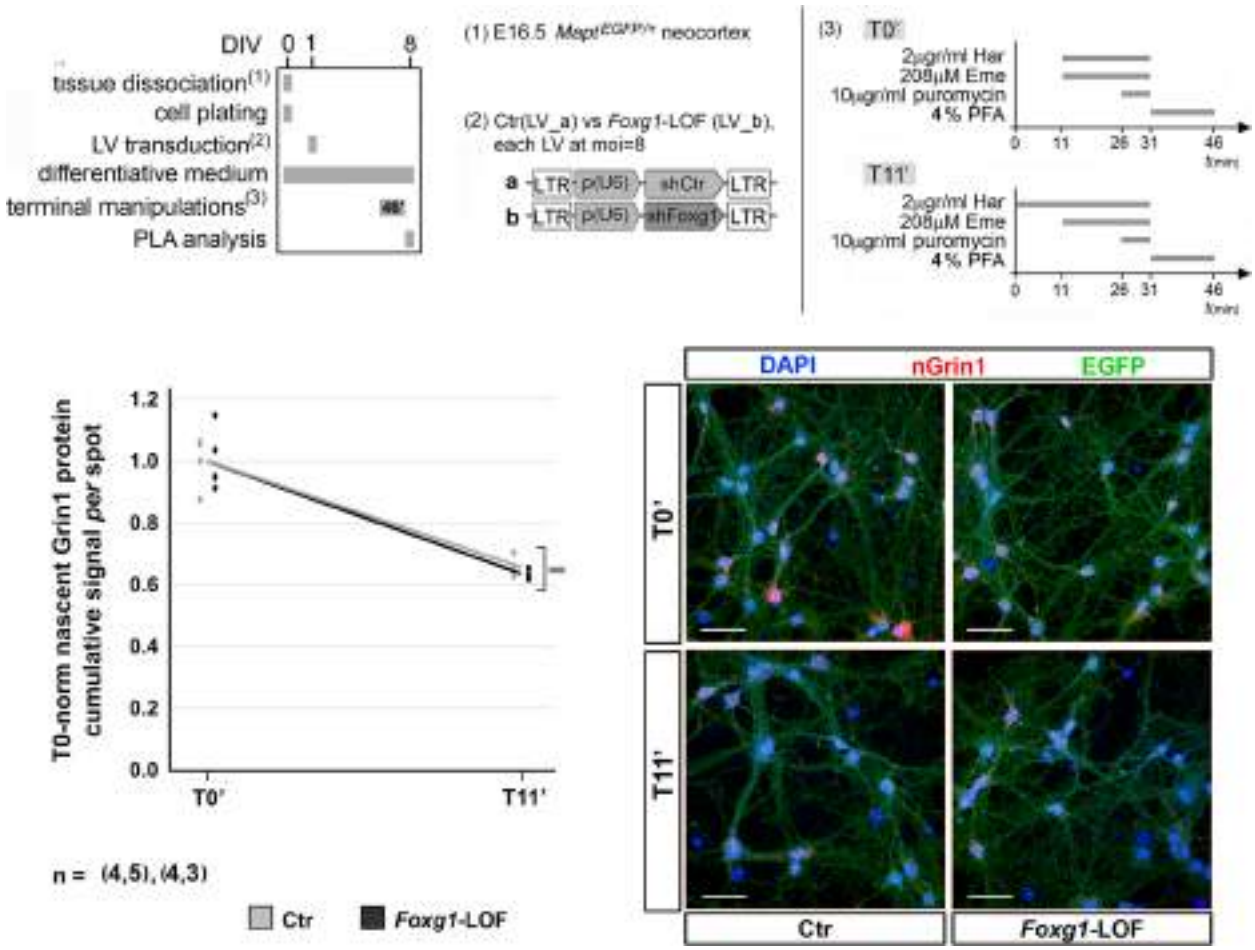

Fig. 4 Evaluation of endogenous pan-GRIN1 elongation rate by run-off assay. To the top, protocols (including lentiviruses employed, and operational details of the translational run-off assay), to the bottom, results. Graph represents progression of nascent GRIN1 levels evaluated by anti-GRIN1-NH2-term/anti-Puromycin-driven PLA, upon *Foxg1* down-regulation, in basal conditions (T0') and 11 min after 2 μg/ml harringtonine (har) blockade of translation initiation (T11'). In both cases, ribosome progression was subsequently inhibited by 208 μM emetine (eme), and nascent polypeptides were terminally labeled by 10 μg/ml puromycin (puro). For each genotype, results normalized against the corresponding average T0' values. Superimposed, linear trendlines. Statistical evaluation of results performed by *t*-test, one-tailed, unpaired, homoscedastic. *n* is the number of biological replicates, i.e., independently cultured and engineered preparations, originating from a common neural cell pool. =, not statistically significant. Included are examples of primary PLA data referred to by the corresponding graphs. Scale bars, 50 μm

modulator"? Results of previous FOXG1 interaction screenings [34–36], our detection of a EIF4E-binding motif-like string within FOXG1 as well as limited responsivity of translation factors' mRNA levels to *Foxg1* overexpression (Additional file 2: Table S1) suggested that type (2) mechanisms might be prevailing.

To preliminarily corroborate this prediction, we engineered HEK293T cells to overexpress FOXG1 and selected translation factors putatively interacting with it (EIF4E, EEF1D, EEF1G, PUM1), and we evaluated their interaction with FOXG1 by proximity ligation assays (PLA). We got evidence that FOXG1 interacts with two of them, EIF4E and EEF1D, implicated in translation initiation and polypeptide elongation, respectively. In case of EIF4E, these results were confirmed by co-immunoprecipitation assays (co-IP). (Additional file 3: Supplementary Results; Additional file 1: Fig. S2A,B).

Next, to assess the biological plausibility of these findings and their relevance to neural genes tuning, we measured the interaction occurring between *endogenous* FOXG1 and *endogenous* EIF4E and EEF1D within primary neocortical cultures, by qPLA (Fig. 5A, B, protocols to left). Compared with technical controls ("anti-FOXG1 only" and "anti-EIF4E only"), the FOXG1/EIF4E assay gave a moderate, however, statistically robust signal. Normalized against controls' average, the number of PLA spots per cell equalled 3.6 ± 0.6 (with $p_{\text{vs-anti}}$-FOXG1-only < 0.01, $p_{\text{vs-anti}}$-EIF4E-only < 0.02

and $n=4,4,4$) (Fig. 5A, graph a), and a similar result was obtained when restricting the analysis to neurites only (PLA signal = 3.2 ± 0.4, with $p_{vs\text{-}anti}$-FOXG1-only < 0.001, $p_{vs\text{-}anti}$-EIF4E-only < 0.02 and $n=4,4,4$) (Fig. 5A, graph b). Evaluated against the corresponding controls ("anti-FOXG1 only" and "anti-EEF1D only"), the FOXG1/EEF1D assay gave an even stronger signal. Normalized against controls' average, the number of PLA-spots per cell equalled 25.1 ± 3.6 (with $p_{vs\text{-}anti}$-FOXG1-only < 0.0003, $p$vs-anti-EEF1D-only < 0.0003 and $n=4,4,4$) (Fig. 5B, graph a), and a similar result was obtained when restricting the analysis to neurites only (PLA signal = 43.8 ± 7.3, with $p_{vs\text{-}anti}$-FOXG1-only < 0.0006, $p_{vs\text{-}anti}$-EEF1D-only < 0.0006 and $n=4,4,4$) (Fig. 5B, graph b). All this suggests that within neocortical neurons (including their neurites), FOXG1 genuinely interacts with both EIF4E and EEF1D.

Finally, to assess the relevance of FOXG1/EIF4E interaction to GRIN1 translation, we outcompeted such interaction by a fragment of the FOXG1 protein and evaluated consequences of this manipulation on GRIN1 synthesis rates. Specifically, by means of a lentiviral vector, we transduced neuronal cultures with a transgene encoding for the mmu-FOXG1 aa357-381 polypeptide, harboring the putative, EIF4E-binding YATHHLT motif. Then, we quantified FOXG1/EIF4E interaction as well as nascent-GRIN1, (n)GRIN1, levels. As expected, compared to a scrambled control, the FOXG1/EIF4E PLA signal was lowered, specifically by −16.3% ± 3.8% (with $p<0.05$ and $n=3,3$) (Fig. 5C, graph a), which resulted into a −29.9% ± 2.7% decrease of (n)GRIN1 ($p<0.02$ and $n=3,3$) (Fig. 5C, graph b). This suggests that the FOXG1/EIF4E interaction contributes to the positive impact exerted by FOXG1 on GRIN1 translation.

FOXG1 physically interacts with *Grin1*-mRNA

To further support the hypothesis that Foxg1 promotes Grin1 synthesis as a translation factor, we investigated if FOXG1 interacts with *Grin1*-mRNA. To this aim, firstly, we quantified the fraction of endogenous *Grin1*-mRNA immunoprecipitated by an anti-FOXG1 antibody in lysates of E16.5 + DIV8 neocortical neurons, by RNA immunoprecipitation (RIP)-qRTPCR (Fig. 6A). This fraction exceeded the IgG background by 17.6 ± 7.4-folds (with $p<0.05$, $n=4,5$) (Fig. 6A, graph a). Upon *Foxg1* knockdown, such fraction also showed a declining trend compared to "wild type" control; however, this was not statistically significant (Fig. 6A, graph b). Then, as an anti-Foxg1 antibody independent control, we scored RNA extracted from neurons overexpressing a FOXG1-EGFP chimera and immunoprecipitated by an anti-EGFP antibody, for *Grin1*-mRNA enrichment. Remarkably, such enrichment equalled 6.1 ± 0.8, upon normalization against PLAP expressing controls (with $p<0.05$, $n=2,2$) (Fig. 6A, graph c). Altogether, these results indicate that within neocortical neurons, *endogenous* Foxg1 protein interacts with *endogenous Grin1*-mRNA.

Next, to identify *Grin1*-mRNA domains needed to bind Foxg1 protein, we co-transduced murine neocortical neurons with Tet^{ON}-controlled, intronless transgenes, encoding for the *Rattus norvegicus Grin1*-203 transcript (including exon 20 and orthologous to the *Mus musculus Grin1*-201 isoform) and artificially deleted variants of it. (Within these transgenes, to prevent toxicity induced by chronic *Grin1* overexpression and potential artifacts due to differential protection of *rnoGrin1*-mRNA by translating ribosomes, a stop codon was inserted between codons 30 and 31 (*rnoGrin1*.203*)). Then, we immunoprecipitated RNA originating from these cultures by

(See figure on next page.)

Fig. 5 Assessment of FOXG1 interaction with EIF4E and EEF1D, and functional relevance of FOXG1-EIF4E interaction to Grin1 translation, in primary cultures of neocortical neurons. **A** PLA assesment of endogenous-FOXG1/endogenous-EIF4E interaction (^{endo}FOXG1-^{endo}EIF4E), in whole neurons, or restricted to neurites. To the left, protocols and lentiviral vectors used, to the right, results. Assays run on cultures of $Mapt^{EGFP}$ neocortical neurons, interaction signals revealed by anti-FOXG1- and anti-EIF4E-driven PLA, performed on whole neurons (graph a) or restricted to their neurites (graph b), according to graphically displayed criteria. Here, graphs report the numbers of spots/cell, normalized against the average of the two corresponding negative controls (each obtained by omitting either primary antibody). **B** PLA assesment of endogenous-FOXG1/endogenous-EEF1D interaction (^{endo}FOXG1-^{endo}EEF1D), in whole neurons, or restricted to neurites. To the left, protocols and lentiviral vectors used, to the right, results. Assays were run on cultures of *wild-type* neocortical neurons, interaction signals were revealed by anti-FOXG1- and anti-EIF4E-driven PLA, and results quantification was performed on whole NeuN-immunoreactive neurons (graph a) or restricted to their neurites (graph b), according to graphically displayed criteria. Here, graphs report the numbers of spots/cell, normalized against the average of the two corresponding negative controls (each obtained by omitting either primary antibody). **C** PLA assesment of ^{endo}FOXG1-^{endo}eIF4E interaction (graph a) and nascent GRIN1 (nGRIN1) levels (graph b) in whole neurons, upon lentivirus-mediated over-expression of a tagged polypeptide including aa357-381 of murine FOXG1 protein (LV_b). A scrambled version of this polypeptide was used as a control (LV_a). To the left, protocols and lentiviral vectors used, to the right, results. Here, shown are cumulative PLA signals per cell, normalized against controls. Throughout the figure, *n* is the number of biological replicates, i.e., independently cultured and engineered preparations, originating from a common cell pool. Statistical evaluation of results performed by *t*-test, one-tailed, unpaired, heteroscedastic (panel **A**(a)) or homoscedastic (panels **A**(b), **B**, and **C**). *$p<0.05$, **$p<0.01$, ***$p<0.001$. Errors bars indicate s.e.m. Throughout the figure, included are examples of primary data referred to by the adjacent graphs. Scale bars, 50 µm

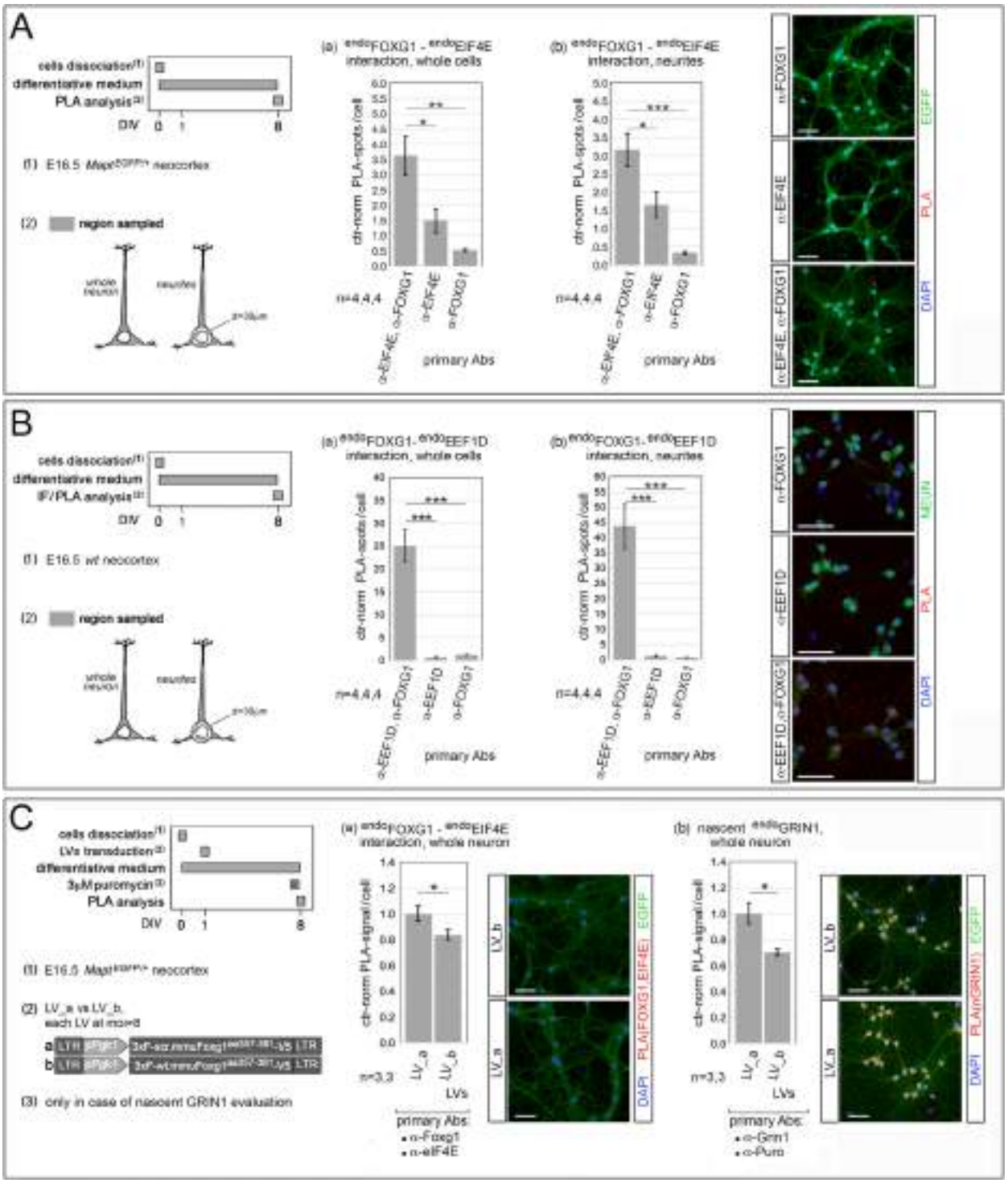

Fig. 5 (See legend on previous page.)

anti-Foxg1 and normalized the IP-*Grin1*-mRNA fraction peculiar to each deletion against the IP fraction of full-length *rnoGrin1*.203*.d0. Finally, we critically evaluated the relevance of distinct *Grin1*-mRNA segments to anti-Foxg1 immuno-precipitability (Fig. 6B). We observed that the two variants missing the AccIII-PshAI fragment at the *Grin1*-cds 3' end, *rnoGrin1*.203*.d3 and *rnoGrin1*.203*.d5, specifically displayed a normalized IP

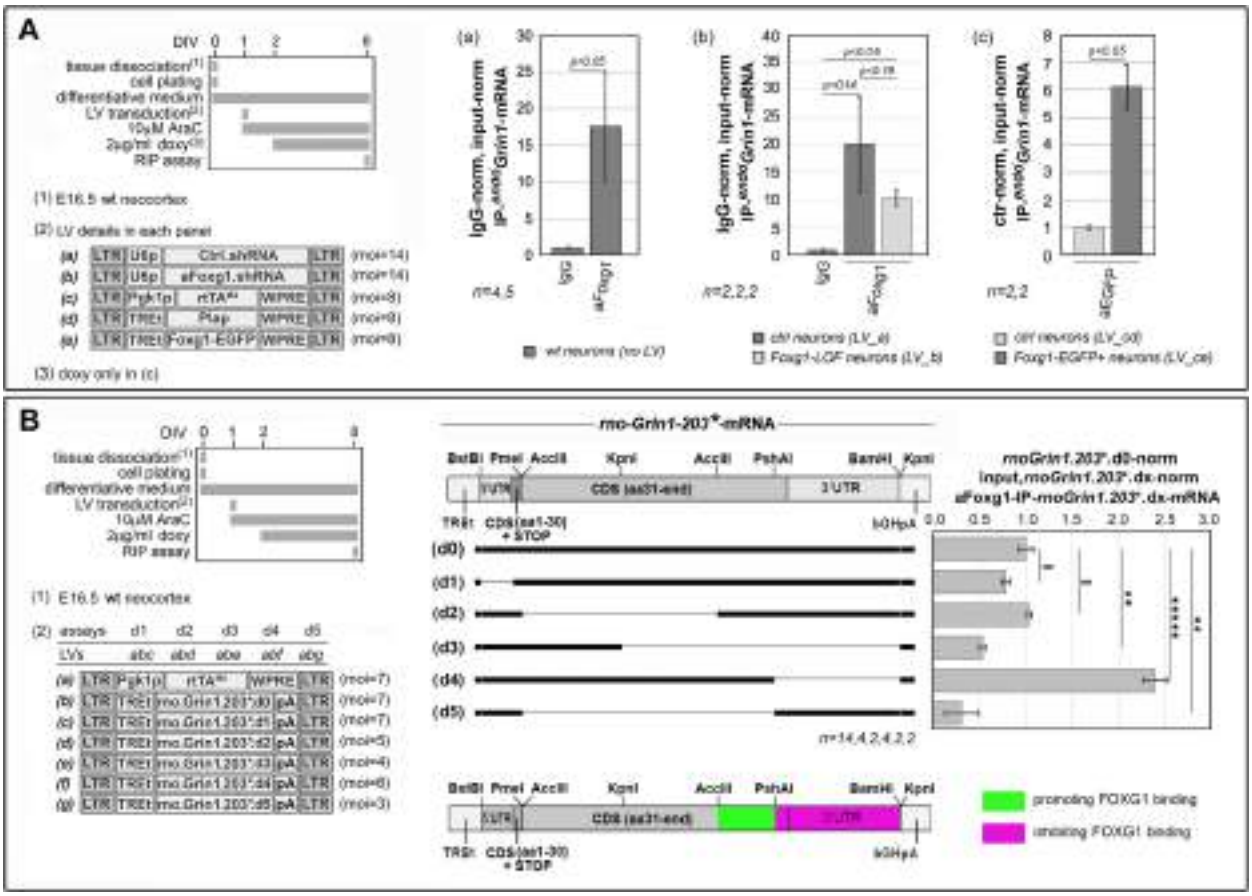

Fig. 6 Evaluation of Foxg1-protein/*Grin1*-mRNA interaction in neocortical neurons, by RNA immunoprecipitation (IP) qPCR (qRIP-PCR) assays. **A** Immuno-precipitation of Foxg1-bound, endogenous *Grin1*-mRNA in neocortical neurons. To the left, protocols and lentiviral vectors used, to the right, results. Anti-Foxg1-IP fraction of endogenous *Grin1*-mRNA in neurons expressing naive (a) or decreased (b) levels of *Foxg1*-mRNA. Results double normalized, against input-RNA and IgG-IP samples. Anti-EGFP-IP fraction of endogenous *Grin1*-mRNA in neurons expressing a lentivector-driven, *Foxg1-EGFP* transgene or a *Plap* control (c). Results double normalized, against input-RNA and control samples. **B** Mapping determinants of Foxg1-protein binding on a heterologous *rno-Grin1*-mRNA, encoded by a lentiviral transgene. To the left, protocols and lentiviral vectors used, to the right, results. Here, a number of partially overlapping deletions were generated starting from the full-length cDNA (d0), by standard molecular cloning techniques, so giving rise to five distinct mutants (d1-d5). To prevent toxicity originating from *chronic*, exaggerated Grin1 expression and potential artifacts stemming from differential protection of *rnoGrin1*-mRNA by translating ribosomes, in all constructs a stop codon was inserted in a fixed position, between codons 30 and 31, so resulting into modified transcripts (*rno-Grin1-203** and derivatives). To quantify the impact of each deletion, neural cultures were co-transduced with lentiviral mixes encoding for different combinations of full-length (d0) and mutant (dx) transgenes. Anti-Foxg1-IP fractions of mutant rno*Grin1*-mRNAs, primarily normalized against the corresponding inputs, were diminished by the corresponding IgG-IP backgrounds and finally renormalized against the average full-length fraction. At the bottom, a color-coded cartoon summarizes the positive or negative impact that distinct transcript domains apparently exert on *Grin1*-mRNA/Foxg1-protein interaction. Throughout the figure, *n* is the number of biological replicates, i.e., independently cultured and engineered preparations, originating from a common neural cell pool. Statistical evaluation of results was performed by *t*-test, two-tailed, unpaired, and homoscedastic. **$p < 0.01$, ***** $p < 0.00001$. Errors bars indicate s.e.m

fraction far below 1 (0.53 ± 0.04 with $p < 0.005$ and $n = 4$, and 0.30 ± 0.19, with $p < 0.005$ and $n = 2$, respectively), pointing to a pivotal role of this fragment in the interaction with Foxg1. On the other side, the removal of the whole 3'UTR, peculiar to *rnoGrin1*.203*.d4, increased the IP fraction up to 2.39 ± 0.13 (with $p < 10^{-5}$ and $n = 2$), suggesting that such domain may normally antagonize Foxg1 recruitment to *Grin1*-mRNA (Fig. 6B). Despite the relatively low number of biological replicates scored, altogether, these results corroborate the specificity of FOXG1/*Grin1*-mRNA interaction and provide a coarse-grained, tentative framework for reconstruction of its regulation. Of course, they do not allow us to make any inference about the topology of such interaction, direct or mediated by an (unknown) bridging effector.

FOXG1 is needed to achieve proper homeostatic tuning of neuronal *Grin1*-mRNA translation

Grin1 is a key player implicated in neuronal plasticity and, in turn, it is the subject of intricate, activity-dependent post-transcriptional regulation [38, 39, 43, 44]. We previously observed that exposing E16.5 + DIV8 neocortical cultures to 55 mM KCl resulted into a dramatic drop of (n)GRIN1 level that was partially rescued upon transferring the same cultures to a low K^+-containing medium. This points to a dedicated mechanism taking care of homeostatic translation tuning (our unpublished results).

To evaluate the relevance of FOXG1 levels to such tuning, we compared the impact of high extracellular K^+ on GRIN1 translation in *Foxg1*-LOF vs wild-type neural cultures (Fig. 7, left). As expected, in wild-type neurons, we confirmed the previously observed collapse of (n)GRIN1 evoked by acute 55 mM K^+ (to 4.4 ± 0.9%o of unstimulated wild-type samples, with $p_{\text{vs-wt-ctr}} < 0.0005$ and $n = 3,3$), as well as the partial rebound of (n)GRIN1 levels upon retransferring cultures to a low K^+ medium (to 59.0 ± 4.3%, with $p_{\text{vs-wt-}}K5' < 0.0002$, $p_{\text{vs-wt-ctr}} < 0.02$, $n = 3,3,3$). Conversely, when *Foxg1* was knocked-down, (a) basal GRIN1 translation was reduced to 49.9 ± 3.7% (with $p_{\text{vs-wt-ctr}} < 0.006$ and $n = 3,3$), (b) the exposure of *Foxg1*-LOF cultures to high K^+ reduced (n)GRIN1 to 9.1 ± 0.8% (normalized against wt_ctr), with $p_{\text{vs-Foxg1.LOF-ctr}} < 0.00003$ and $n = 3,4$, and (c) the subsequent re-transfer of these cultures to standard potassium allowed (n)GRIN1 to rebound to 27.3 ± 7.2% (again normalized against wt_ctr), with $p_{\text{vs-Foxg1.LOF-K5}'} < 0.03$, $p_{\text{vs-Foxg1.LOF-ctr}} < 0.03$, and $n = 3,4,4$ (Fig. 7, right). In other words, compared to controls, *Foxg1* knock-down dampened the early homeostatic response to high K^+ by about fourfolds (4.4% vs 100.0% and 9.1% vs 49.9%, respectively, with p(genotype/K+)interaction < 0.002, as assessed by two-way ANOVA).

To sum up, we found that GRIN1 de novo synthesis undergoes a prominent and reversible, homeostatic regulation, and FOXG1 is instrumental to that.

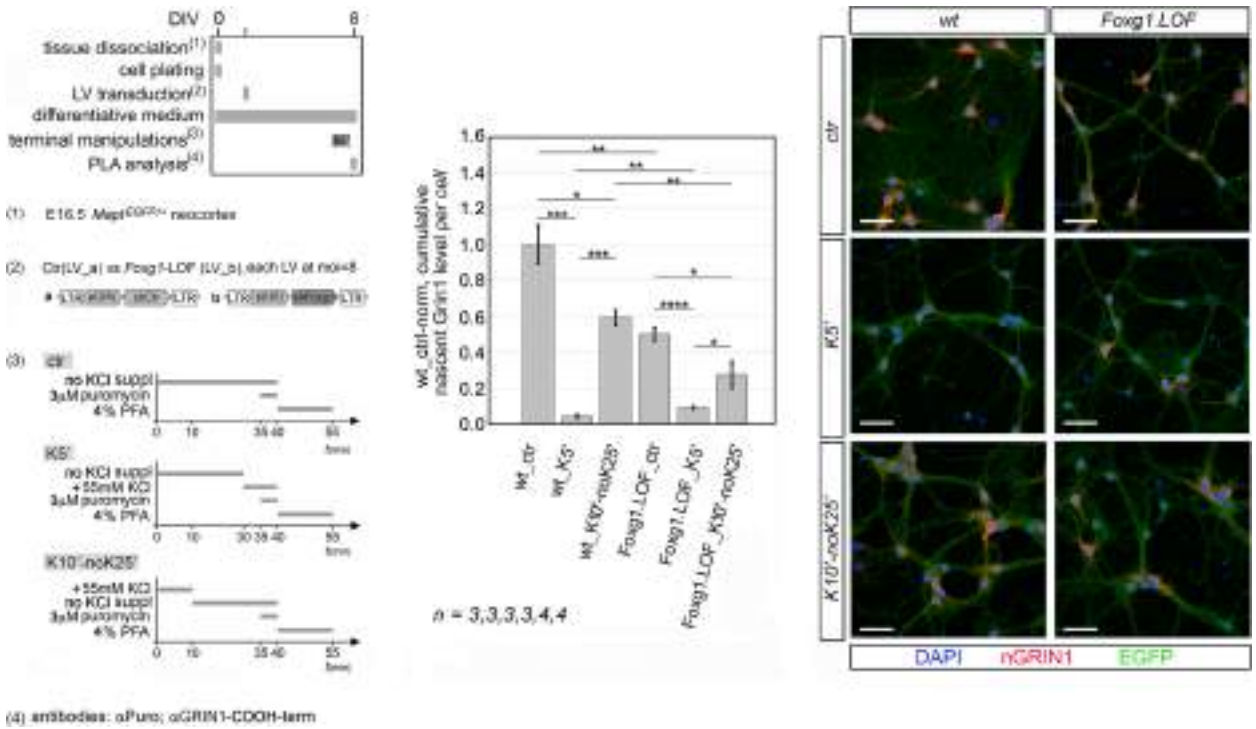

Fig. 7 Foxg1 relevance to homeostatic *Grin1*-mRNA translational tuning. To the left, protocols (including lentiviruses employed, and operational details of transient neuronal stimulation), to the right, results. Impact of *Foxg1*-down-regulation on (n)Grin1 levels, following acute exposure of neocortical neurons to high extracellular potassium (*K5'*) and their return to not-K^+-supplemented medium (*K10'-noK25'*). *Foxg1* knockdown elicited via shRNA-encoding lentivirus. (n)Grin1 evaluated by anti-Grin1-COOH-term/anti-puromycin-driven proximity ligation assay (PLA). Results normalized against unstimulated controls (*wt_ctr*). Included are examples of primary data. *n* is the number of biological replicates, i.e., independently cultured and engineered preparations, originating from a common cell pool. Scale bars, 50 µm. Statistical evaluation of results performed by *t*-test, one-tailed, unpaired, and homoscedastic, and two-way ANOVA. =, not statistically significant, *$p < 0.05$, **$p < 0.01$, ***$p < 0.001$, ****$p < 0.0001$. Errors bars indicate s.e.m

Widespread impact of FOXG1 on mRNA engagement to ribosomes

We wondered if *Foxg1* impact on translation is peculiar only to a few genes including *Grin1* or is it a pervasive phenomenon. To get an insight into this issue, we systematically sequenced ribosome-engaged-mRNA (trapRNAseq) purified from *Foxg1*-OE and control cultures (as in Fig. 2A, to left) and compared it to total-mRNA originating from corresponding sister cultures (totRNAseq) [17].

For simplicity's sake, we took into account trapRNAseq and totRNAseq reads belonging to the only principal isoform of each gene (according to APPRIS annotation) [45]. We calculated log2 "expression fold change" values (log2FC) peculiar to trapRNA and totRNA samples and evaluated statistical significance of results by DESeq2 software [46]. Next, we scored each gene on the basis of the "log2FC(trapRNAseq)-log2FC(totRNAseq)" difference (hereafter Δlog2FC), as a measure of FOXG1-dependent stimulation of ribosomal mRNA engagement and a presumptive index of FOXG1-driven promotion of its translation. Finally, we evaluated statistical significance of results by Ribodiff software [47].

Upon filtering out low-expressed genes as well as those with $p_{adj} \geq 0.1$, we found 183 genes with Δlog2FC > 0.5 (i.e., with FOXG1 presumptively promoting their translation) and 175 genes with Δlog2FC < -0.5 (i.e., with FOXG1 presumptively antagonizing their translation). Categorized by Δlog2FC value, these genes largely fell within the "1.0 to 1.5" and the "−1.5 to −1.0" intervals (66 and 72 genes, respectively) (Fig. 8A; Table 1; Additional file 4: Table S2A). As shown by GO analysis, such genes preferentially encode for proteins (a) involved in synaptic signaling, behavior, memory, and fatty acid catabolism, (b) localized at the plasma membrane and synapses, and (c) acting as channels, neurotransmitter receptors, transmembrane transporters, and transcription factors (Additional file 4: Table S2B).

Next, we further classified these genes as for their *Foxg1*-driven totRNA dynamics. We found that among 183 genes with increased ribosomal engagement, as many as 118 displayed reduced totRNA and only 14 increased totRNA. Symmetrically, among 175 genes with decreased ribosomal engagement, 117 and 5 had upregulated and downregulated totRNA, respectively (Fig. 8B). All that results in a variegated scenario, as shown in Fig. 8C.

Next, to exclude possible artifactual results originating from FOXG1-dependent alteration of pre-mRNA maturation, we re-analyzed primary totRNA data [18] by CASH [48] and ROAR [49] softwares. Interestingly, we found that, upon FOXG1 overexpression, only (7 + 14) = 21 of the (183 + 175) = 358 genes "with altered ribosomal engagement" mentioned above displayed altered splicing and polyadenylation, respectively (Table 1; Additional file 4: Table S2A).

Then, to further corroborate our findings, we systematically interrogated mRNAs "with altered ribosomal engagement" for a possible interaction with the FOXG1 protein. For this purpose, we relied on sequencing of RNA extracted from E16.5 + DIV8 pallial cultures and immunoprecipitated by an anti-FOXG1 antibody, taking selectively into account exonic reads representative of mature mRNAs (here we referred to the principal splicing isoform, according to APPRIS annotation [45]). We monitored the distribution of these reads by Sicer software, comparing anti-FOXG1-IP samples with IgG-treated controls. FOXG1/mRNA interaction peaks with anti-FOXG1/IgG_enrichment ≥ 2 and fdr < 0.05 resulting from this analysis were further taken into account, and mRNAs sharing ≥ 1 peak in ≥ 2 out of 3 biological replicates were considered as interacting with the FOXG1 protein. Specifically, 2857 distinct mRNAs fulfilled this requirement and, interestingly, among the 358 genes "with altered ribosomal engagement" mentioned above, as many as 138 encoded for them (Table 1; Additional file 4: Table S2A).

PuroPLA validation of presumptive translational targets of FOXG1

To validate the bioinformatic procedure described above, we selected *Sgk1* and *Homer1*, namely two genes presumptively undergoing a robust *Foxg1*-OE-driven translational enhancement (Δlog2FC equaling +1.89, with $p_{adj} < 0.04$, and +1.56, with $p_{adj} < 0.01$, respectively) in the face of a significative downregulation of the corresponding mRNAs (−24.94%, with $p < 10^{-4}$, and −46.24%, with $p < 10^{-21}$, respectively), and we monitored the synthesis rate of their protein products in *Foxg1*-OE neurons by puro-PLA. We found that, compared to controls, such rate was increased in the case of *Sgk1* (by 3.09 ± 0.54-folds, with $p < 0.012$ and $n = 4,4$), and barely shifted upward in the case of *Homer1* (1.12 ± 0.15, $p = 0.28$, $n = 5,5$). Taking into account the underlying declining mRNA dynamics, these results unambiguously point to a positive *Foxg1* impact on both *Sgk1* and *Homer1* translation gains. Conversely, the translation rate of NMT1, displaying no statistically significant Δlog2FC value or variation in ^{tot}mRNA level, was not affected upon *Foxg1* overexpression (Fig. 9A-C).

Moreover, to confirm that the differences observed among protein and mRNA dynamics upon *Foxg1* manipulation were due to a direct FOXG1 impact on translation, we considered to overexpress a cytoplasm-confined variant of FOXG1 and assay its impact on neuronal rates of SGK1 translation. For this purpose, we generated a Tet^{ON}-controlled *Foxg1-Ert2-Flag-V5* transgene encoding

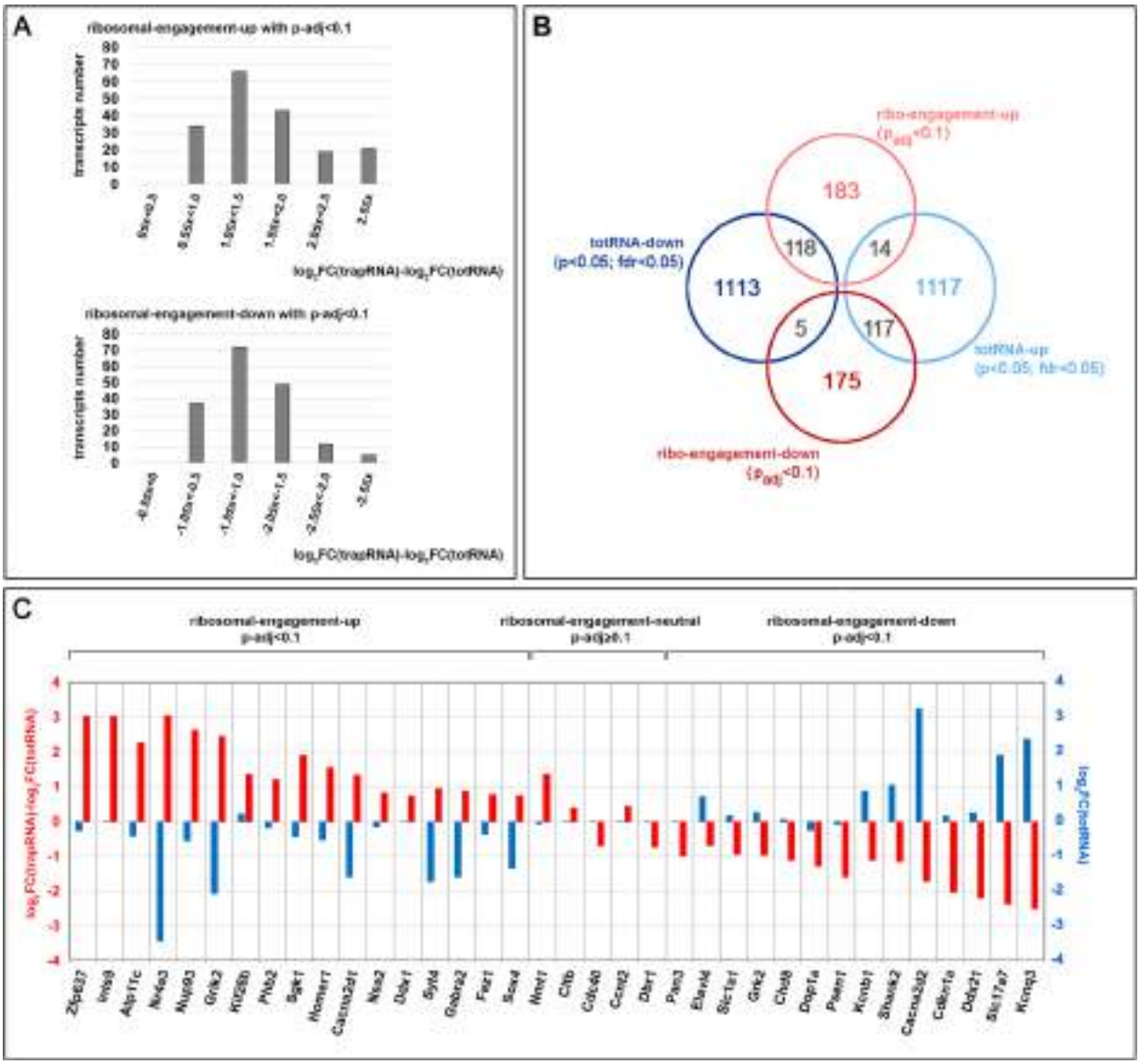

Fig. 8 Evaluation of Foxg1 impact on ribosomal mRNA engagement by TRAP-Seq/RNA-Seq. **A** Transcripts distribution by "log2FC(trapRNAseq)-log2FC(totRNAseq)" (or Δlog2FC). To the top, transcripts with Δlog2FC > 0 and *p*adj < 0.1 ("ribosomal engagement up"), to the bottom transcripts with Δlog2FC < 0 and *p*adj < 0.1 ("ribosomal engagement down"), **B** Venn's diagram representation of genes distribution among the four categories: "ribo-engagement-up" (Δlog2FC > 0 and *p*adj < 0.1), "ribo-engagement-down" (Δlog2FC < 0 and *p*adj < 0.1), "totRNA-up" (log2FC > 0, with $p < 0.05$ and fdr < 0.05), and "totRNA-down" (log2FC < 0, with $p < 0.05$ and fdr < 0.05). **C** Representative examples of genes falling in the three categories: "ribosomal engagement up", "ribosomal engagement neutral" (i.e., with *p*-adj ≥ 0.1), and "ribosomal engagement down". Here, for each gene plotted are "log2FC(trapRNAseq)-log2FC(totRNAseq)" and "log2FC(totRNAseq)"

for a chimeric polypeptide, which included FOXG1, the estrogen receptor-derivative ERT2 module (confining the polypeptide to cytoplasm [50, 51]), as well as Flag and V5 epitopes (for immunolocalization) (Additional file 1: Figure S4A, B). We delivered this transgene (as well as its *Plap* and *Foxg1* controls) to primary neocortical cultures, by lentiviral vectors (Fig. 9D). As expected, we observed a confinement of V5 immunofluorescence to cytoplasm, which was specifically abolished upon 4-hydroxytamoxifen (4OHT) supplementation (Fig. 9E). Interestingly, we found that, while not affecting expression levels of two mRNAs which are highly sensitive to wild-type FOXG1 (*Gad1* and *Arc*) (Fig. 9F, G), *Foxg1-Ert2-Flag-V5* stimulated SGK1 translation (Fig. 9F, H, I). Compared to *Plap* controls, it increased the cumulative PuroPLA-SGK1 signal per neuron by 1.92 ± 0.14 ($p < 0.008$, $n = 3,4$),

Table 1 Distribution of Foxg1-sensitive splicing, Foxg1-sensitive polyadenylation, and mRNA interaction with Foxg1 protein, among gene transcripts characterized by altered ribosomal engagement and/or progression upon *Foxg1* over-expression

	Total	With altered splicing[3]	With altered polyadenylation[4]	With Foxg1-interacting mRN[5]
Genes with altered ribosomal engagement[1]	358	7	14	138
Genes with altered ribosomal progression[2]	328	6	17	93

[1] Identified by integrated evaluation of totRNA-Seq and TRAP-Seq data; satisfying "$\Delta\log_2FC \neq 0$; $p_{adj} < 0.1$"

[2] Identified on the basis of distribution of TRAP-Seq-reads along every transcript; satisfying "f_{boi}-zscore ≥ 3"

[3] Identified by cash software, with $-0.1 \geq \Delta psi \geq 0.1$;fdr < 0.05

[4] Identified by roar software, with $1/1.2 \geq r \geq 1.2$; fdr < 0.05

[5] Identified by aFoxg1RIP-Seq, based on the occurrence of Foxg1-protein/mRNA interaction peaks with aFoxg1/IgG_enrichment ≥ 2 and fdr < 0.1 (mRNAs taken into account sharing ≥ 1 peak in ≥ 2 out of 3 biological replicates; calculations restricted to the main isoform of each mRNA)

similarly to what was achieved by its *Foxg1* counterpart (2.25 ± 0.30-folds, with $p < 0.005$, $n = 3,4$). This confirms a *direct* impact of FOXG1 on translation, independent from its transcription factor activity.

FOXG1 impact on ribosome progression along mRNAs

We further mined our TrapSeq data, aiming at unveiling a possible impact of *Foxg1* expression levels on ribosomal progression along mRNAs. For this purpose, we assumed that because of random mechanical fragmentation undergone by "ribo-trapped" mRNA during the immunoprecipitation procedure, reads location should provide information about the position occupied by the 60S subunit along the mRNA-cds. Specifically, for each gene, we took into account the principal isoform (according to APPRIS annotation) [45], and, for each transcript, we allotted reads to adjacent 125 base-wide cds bins. Next, considering each bin/bin boundary as a potential bottleneck for ribosome advancement, we calculated the corresponding ribosome progression index (rpi), as the ratio among reads falling downstream and upstream of such boundary (Fig. 10A). For each boundary, we averaged rpis of the three *Foxg1*-OE replicates and those of the four controls, and we annotated boundaries with log2FC(rpi) ≥ 1 and $p < 0.05$ as "boundaries of interest, up" (boi.ups). Then, we evaluated the frequency of such boundaries over the full cds ($f_{boi.up}$), as a global, gene-specific index of *Foxg1*-dependent *promotion of* ribosomal progression. In parallel, referring to boundaries with log2FC(rpi) ≤ -1 and $p < 0.05$ (boi.downs), we similarly obtained an alternative, gene-specific index of *Foxg1*-dependent *inhibition of* ribosomal progression ($f_{boi.down}$). Finally, to deal with potential false positives originating from random non-*Foxg1*-dependent variability of ribosome progression, we built all the 34, (4 + 3)-type permutations of our sample sets and, on each permutation, we repeated the above-described analyses. At the end, for each gene, we calculated the $f_{boi.up}$ and $f_{boi.down}$ z-scores, and we filtered out potential candidates with z-scores < 3 (Fig. 10A; Table 1; Additional file 4: Table S2C). Among genes with z-scores ≥ 3 (likely undergoing *Foxg1*-dependent modulation of ribosomal progression), 165 harbored at least one boundary with log2FC(rpi) ≥ 1 and $p < 0.05$ (boi.up), conversely 163 displayed at least one boundary with log2FC(rpi) ≤ -1 and $p < 0.05$ (boi.down). In both cases, the z-score distribution was relatively flat and the correlation between z-score and median log2FC(rpi) very low (Fig. 10B). As expected, moving from low to high f_{boi} z-score genes, we found a progressively more pronounced differential distribution of reads, preferentially clustered towards the *Foxg1*-OE cds-3' in boiup-rich genes and towards the control cds-3' in boidown-rich ones (Fig. 10C). As shown by GO analysis, genes characterized by FOXG1-modulated ribosome distribution along their transcripts preferentially encode for proteins implicated in fatty acid catabolism, Na^+ binding, AMP binding, and serine/threonine kinase activity (Additional file 4: Table S2D).

Again to exclude possible artifactual results originating from *Foxg1*-dependent alteration of pre-mRNA maturation, we monitored results of CASH and ROAR profiling of total RNA from *Foxg1*-OE and control neocortical cultures. Interestingly, we found that upon *Foxg1* overexpression, only $(6 + 17) = 23$ of the $(165 + 163) = 328$ genes "with altered ribosomal progression" mentioned above displayed altered splicing and polyadenylation, respectively (Table 1; Additional file 4: Table S2C).

Then, to further corroborate our findings, we intersected such $(165 + 163) = 328$ genes "with altered ribosomal progression" with the 2857 ones encoding for FOXG1-interacting mRNAs, previously identified by anti-FOXG1-RIP/Seq. Interestingly, it turned out that 46/165 and 47/163 genes "with altered ribosomal progression" encoded for FOXG1-interacting mRNAs (Table 1; Additional file 4: Table S2C).

PuroPLA run-off validation of presumptive FOXG1 impact on ribosomal progression

Finally, to assess the validity of our bioinformatic approach to identify candidate genes affected by FOXG1-dependent differential ribosomal progression along their mRNAs, we evaluated translation rates of *Camk2b* and

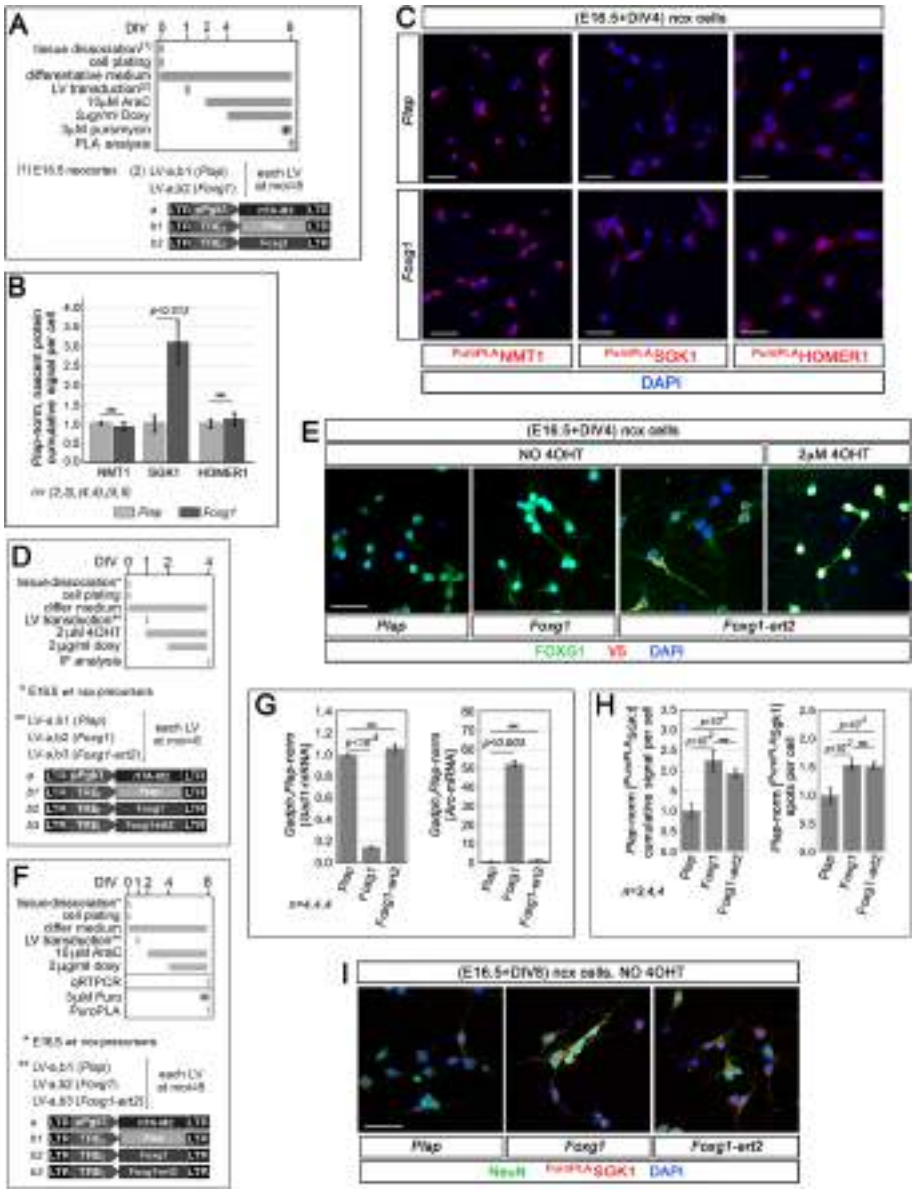

Fig. 9 Experimental validation of FOXG1 impact on translation rates, upon its generalized or cytosol-confined overexpression in primary neocortical cultures. **A**–**C** Validation of FOXG1 impact on translation rates upon *generalized* FOXG1 overexpression. In **A**, protocol, including lentiviral vectors for Tet^{ON}-controlled overexpression of the *Foxg1* transgene and its *Plap* control. In **B**, quantification of nascent NMT1, SGK1, and HOMER1 proteins in engineered cultures, as revealed by anti-protein/anti-puromycin-driven, proximity ligation assay (PLA), and confocal immunofluorescence (IF). Specifically, shown are average cumulative signals per cell. In **C**, examples of primary data referred to in **B**. Scale bar, 50 µm. **D**, **E** Assaying restriction of the FOXG1-V5-FLAG-ERT2 chimera to cytoplasm of neocortical neurons harboring a *Foxg1-V5-Flag-Ert2* transgene. In **D**, protocol, including lentiviral vectors driving Tet^{ON}-controlled expression of the *Foxg1-V5-Flag-Ert2* transgene (abbreviated as *Foxg1-ert2*) or its controls (*Plap* and *Foxg1*). In **E**, co-profiling of engineered cultures for FOXG1 and V5 (as expected, the V5 signal is basically confined to cytoplasm, and a displacement of it to nucleus takes place upon 4-hydroxytamoxifen (4OHT) medium supplementation). Scale bar, 50 µm. **F**–**I** Validation of FOXG1 impact on translation rates upon *cytosol-confined* FOXG1 overexpression. In **F**, protocols, including lentiviral vectors for Tet^{ON}-controlled overexpression of the *Foxg1-ert2* transgene and its *Plap* and *Foxg1* controls. In **G**, **H** results. The engineered cultures were profiled for **G** *Gad1*- and *Arc*-mRNA levels, by qRTPCR, as well as for **H** SGK1 translation rates, by PuroPLA and IF. Results were normalized against **G** *Gapdh* and *Plap* controls and **H** *Plap* controls. In **I**, examples of primary data referred to in **H** graphs. Scale bar, 50 µm. In **B**, **G**, **H**, *n* is the number of biological replicates, i.e., independently cultured and engineered preparations, originating from a common cell pool. Statistical evaluation of results performed by *t*-test, one-tailed, unpaired, and homoscedastic (panels **B** (NMT, HOMER1), **G** (*Gad1*), **H** (right)) or heteroscedastic (panels **B** (SGK1), **G** (*Arc*), **H** (left)). Error bars indicate s.e.m

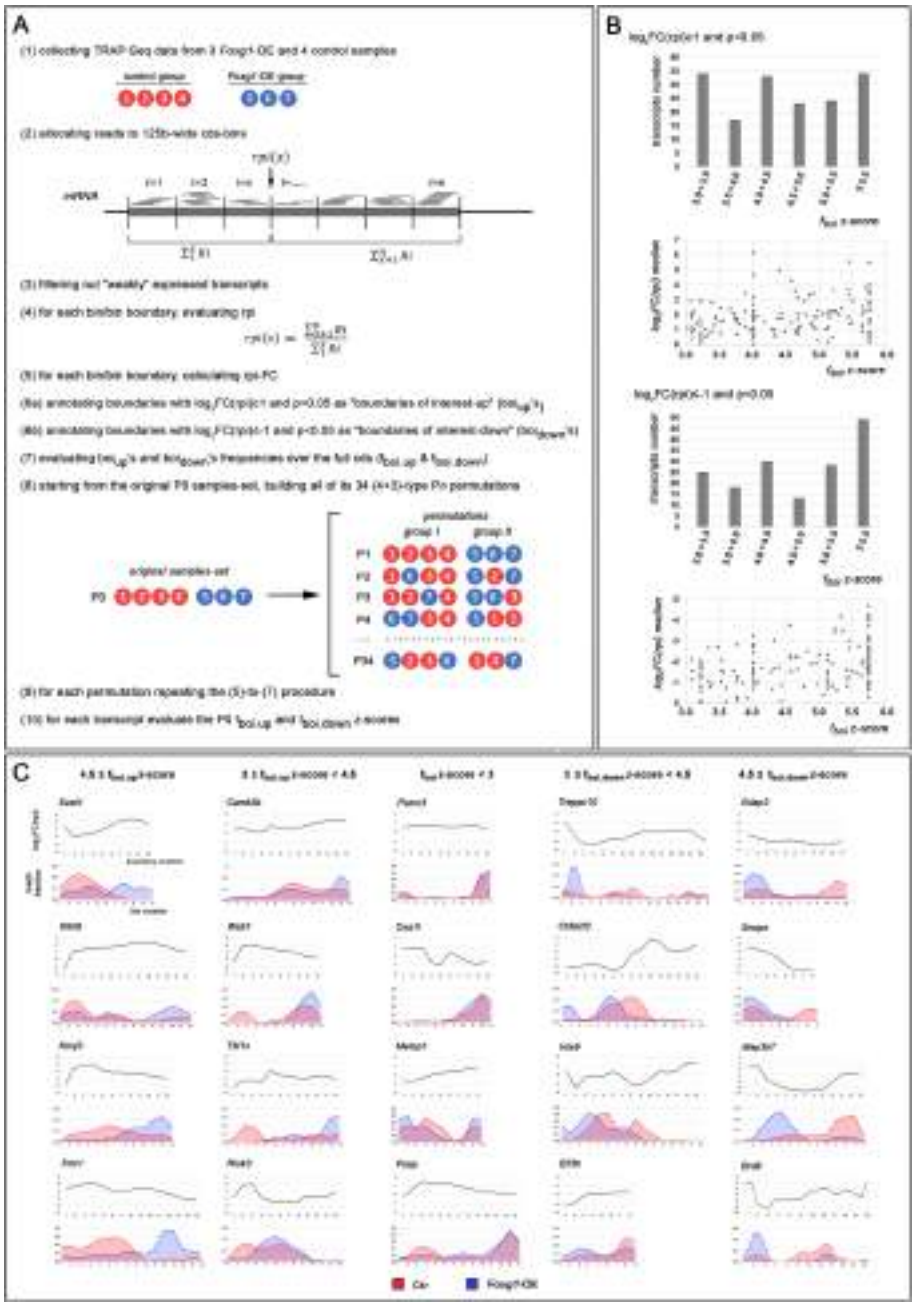

Fig. 10 Evaluation of Foxg1 impact on ribosome progression along mRNA by TRAP-seq. **A** Step-by-step protocol for *Foxg1*-OE TRAP data mining. Here, *Ri* indicates the number of reads mapped within the #i bin; *n* is the total bin number; *rpi* is the "ribosome progression index". **B** Transcripts distribution by *f*boiz-score, and correlation between *f*boiz-score and median log2FC(rpi), as evaluated for transcripts with "log2FC(rpi) ≥ 1, $p < 0.05$" (top graphs) and "log2FC(rpi) ≤ -1, $p < 0.05$" (bottom graphs). **C** Examples of genes falling in five different categories, on the basis of their fboiz-score values. For each gene, shown are log2FC(rpi) progression against bin/bin boundary number (top graph) and reads fraction progression against bin number (bottom graph)

Fmr1, namely two boi.up-rich genes (with "$3.0 \leq f_{\text{boi.up}}$ z-score < 4.5" and "$f_{\text{boi.up}}$ z-score > 4.5", respectively), characterized by diversified reads distributions along their cds in *Foxg1*-OE vs control samples (Fig. 10C) and mRNA expression levels not affected upon *Foxg1* manipulation (Additional file 5: Table S3B). For this purpose, we employed a dedicated puro-PLA run-off assay, similar to the one used for GRIN1 (Figs. 4 and 11A; Additional file 1: Figure S3). In the case of CAMK2B, upon setting the *ti* time to 4.5 min, we found that the

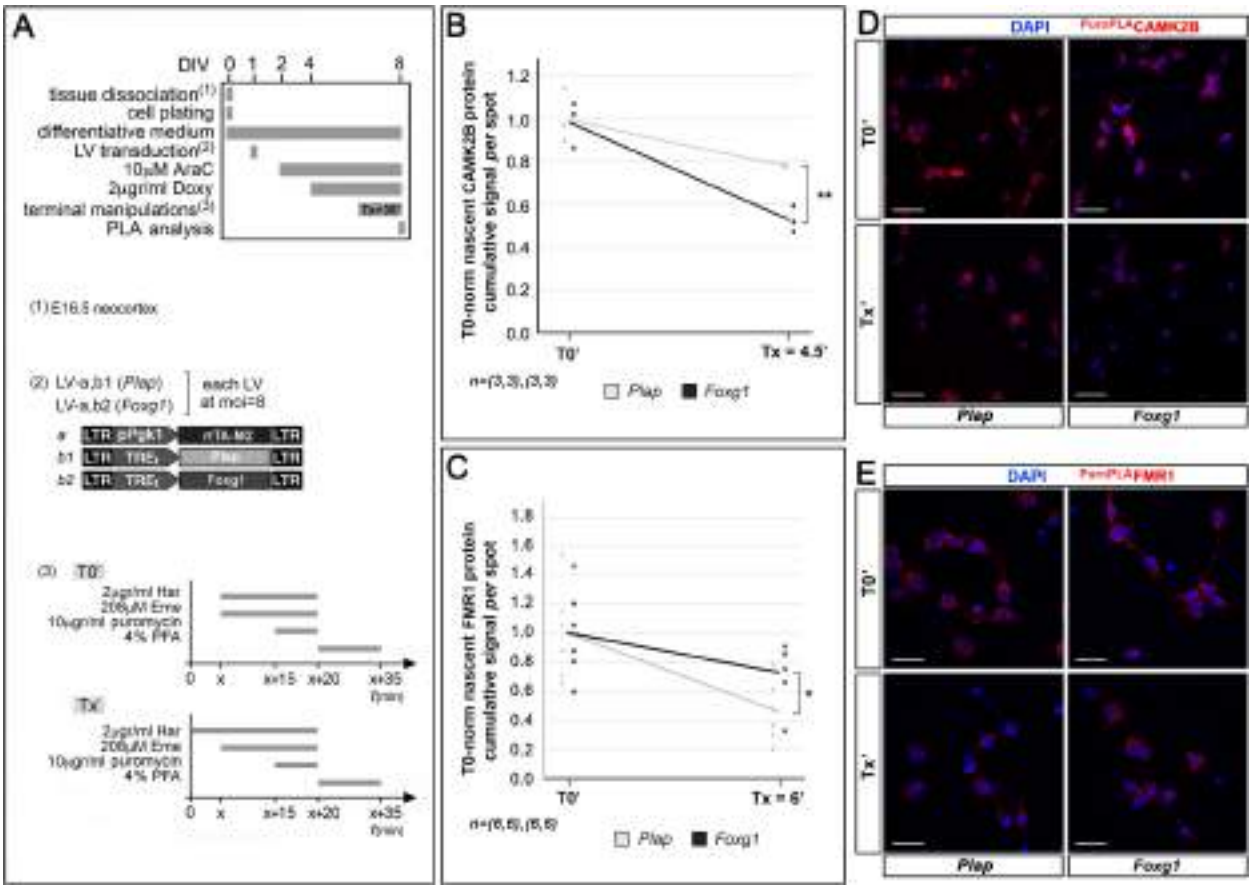

Fig. 11 Experimental validation of ribosome progression profiles, inferred from distribution of TRAP-seq reads along mRNAs in *Foxg1*-OE samples. **A** Protocols, including lentiviruses employed, and operational details of the translational run-off assay. **B**, **C** Results. Graphs represent progression of nascent CAMK2B and FMR1 levels, evaluated by anti-CAMK2B or anti-FMR1/anti-Puromycin-driven PLA, upon *Foxg1* up-regulation, in basal conditions (T0') as well as 4 min and 30 s (case CAMK2B) or 6 min (case FMR1) after 2 μg/ml harringtonine (har) blockade of translation initiation (Tx'). In both cases, ribosome progression was subsequently inhibited by 208 μM emetine (eme), and nascent polypeptides were terminally labeled by 10 μg/ml puromycin (puro). For each genotype, results normalized against (T0') average values. Superimposed, linear trendlines. Statistical evaluation of results performed by *t*-test, one-tailed, unpaired, homoscedastic. $*p < 0.05$; $**p < 0.01$. Errors bars indicate s.e.m. *n* is the number of biological replicates, i.e., independently cultured and engineered preparations, originating from a common neural cell pool. **D**, **E** Examples of primary data referred to by graphs in **B** and **C**, respectively. Scale bars, 50 μm

t0-normalized decline of the PLA signal (−22.2 ± 0.2% in controls) was remarkably exacerbated in *Foxg1*-OE samples (−47.2 ± 3.5% with $p < 0.002$ and $n = 3,3$) (Fig. 11B, D). This points to an overt positive impact exerted by FOXG1 overexpression on ribosome progression along *Camk2b*-mRNA. It provides a first positive assessment of the predictive power of the bioinformatic strategy we employed. Vice versa, in the case of FMR1, upon setting the *ti* time to 6 min, we found that the *t0*-normalized decline of the PLA signal (−54.5 ± 8.7% in controls) was *reduced* in *Foxg1*-OE samples (−27.3 ± 8.8% with $p < 0.027$ and $n = 6,6$) (Fig. 11C, E). It is possible that in this case, rather than simply originating from faster holoribosome progression through the very body of the cds, the preferential clustering of ^{trap}mRNA reads detectable in the 3' half of it upon *Foxg1*-OE might reflect some preterminal holoribosome accumulation, due to an alternative, 3'-terminal bottleneck evoked by this treatment (Fig. 10C).

Discussion

Here, inspired by the detection of FOXG1 protein in neuritic cytoplasm of pallial pyramids (Fig. 1; Additional file 1: Figure S5), we investigated its potential implication in the translation of selected neuronal genes, and we documented an impact of *Foxg1* on ribosomal engagement of *Grin1*-mRNA (Fig. 2A, B). Next, we showed that FOXG1 increases GRIN1 protein level by enhancing translation of its mRNA, while not ameliorating its stability (Figs. 2C–F and 3). Such enhancement

was apparently due to increased translational initiation (Fig. 4). Mechanisms underlying these phenomena included FOXG1 protein interaction with EIF4E (Fig. 5) and, possibly, *Grin1*-mRNA (Fig. 6). Moreover, we found that *Grin1*-mRNA translation undergoes a prominent (and reversible) homeostatic regulation and FOXG1 is instrumental to that (Fig. 7). Finally, a dedicated TRAP-seq survey showed that functional FOXG1 implication in translation control (both initiation and ribosome progression) is a pervasive phenomenon, affecting hundreds of neuronal genes. In selected cases, we experimentally verified such implication (Figs. 8, 9, 10, and 11).

The localization of FOXG1 in early-born neocortical glutamatergic neurons outside of the nucleus, had been already reported [32]. Here we showed that FOXG1 is specifically detectable in soma, dendrites, and axons of the majority of pallial pyramids, including the mitochondria as well as the cytoplasm (Fig. 1).

Based on higher *Grin1*-mRNA levels detectable in ribosome-engaged compared to not-ribosome-engaged-RNA of *Foxg1*-OE neurons (Fig. 2B), we inferred a likely positive impact of FOXG1 on GRIN1 translation. However, enhanced recruitment of an mRNA to ribosomes, as documented by TRAP analysis, does not imply per se an increased synthesis of its protein product, but it could alternatively reflect enhanced stalling of the holoribosome on such mRNA, ultimately resulting in *reduced* protein outcome of translation. To disambiguate this issue, we subsequently compared levels of *Grin1* mRNA and protein. We found that higher *Foxg1* levels led to increased "GRIN1-protein to *Grin1*-mRNA" ratios (Fig. 2F) in the absence of GRIN1-protein stabilization (Fig. 3C). Moreover, we found that they resulted in increased puromycin-tagged, nascent GRIN1 (Fig. 3A). All that allowed us to definitively validate the aforesaid inference. Intriguingly, a substantial fraction of nascent GRIN1 was detected in neurites (Fig. 3A), consistently with previously reported localization of the corresponding mRNA in these structures [52–55]. To notice, *Foxg1* did not drive any appreciable, generalized enhancement of translation (Fig. 3B).

The synthesis rate of a given polypeptide does not depend only on the initiation of its translation, but it also reflects the speed at which it is elongated. In this respect, combined use of harringtonine and puromycin had already been employed to assay cumulative, proteome-wide polypeptide elongation rates [42]. Here, by means of PLA, we re-adapted this method to evaluate elongation rates of *specific* polypeptides in distinctive sub-cellular locales (Additional file 1: Figure S3). Albeit technically working (Fig. 11), this approach did not allow us to document any *Foxg1*-driven change of this rate in the case of GRIN1 (Fig. 4).

As for molecular mechanisms underlying FOXG1 impact on *Grin1* translation, we achieved multiple pieces of evidence pointing to it as a "translation modulator". In fact, beyond its detection in neuronal cytoplasm (Fig. 1), we found that FOXG1 interacts with EIF4E, and partial inhibition of its interaction with the latter resulted in a substantial decline of Grin1 translation (Fig. 5). Moreover, FOXG1 binds to *Grin1*-mRNA (Fig. 6).

To note, whereas our PLA-based investigation of FOXG1/EEF1D association confirmed in pallial neurons results achieved by means of high-throughput mass spectrometry (MS) screenings previously run in HEK293T and N2A cells [34, 36], conversely, the FOXG1 interaction with EIF4E, which we proved by both IP-WB analysis and PLA (Fig. 5A; Additional file 1: Figure S2), is novel. Moreover, while an interaction of FOXG1 with ncRNAs (miRNA precursors) had been previously reported [36], FOXG1 interaction with mRNA has been only recently described, however as a retrotransposition-related phenomenon [56]. Needless to say, FOXG1 association to EIF4E and EEF1D resonates with presumptive FOXG1 implication in translation initiation (Fig. 8) and polypeptide elongation (Fig. 10), respectively [57, 58].

It has been shown that acute stimulation of hippocampal pyramids by high extracellular potassium may evoke a fast increase of cap-dependent translation [59]. Moreover, *Grin* genes—which encode for subunits of the heteromeric NMDA receptor—undergo an intricate, multi-step regulation needed for proper setting of integrative properties of neocortical pyramids [44]. In this context, specific and reversible high K^+-driven *downregulation* of GRIN1 translation (Fig. 7) might represent the experimental correlate of specific physiological mechanisms contributing to homeostatic scaling of neuronal response to glutamate [39].

Next, *Foxg1* has been recently shown to promote activity and excitability of neocortical neurons, largely via a profound impact on their transcriptome [17]. Consistently, FOXG1-depleted hippocampal neurons display reduced NMDA currents and defective long-term potentiation (LTP) [15]. In this respect, *Foxg1*-dependent modulation of GRIN1 translation (Figs. 3 and 7) might be a key mechanism concurring to both these effects.

Finally, we have recently shown that *Foxg1* is transiently upregulated by neuronal hyperactivity [17, 19]. In this way, delayed FOXG1-mediated promotion of GRIN1 translation, following episodes of intense electrical activity, might contribute to normal dynamic shaping of pyramid excitability, and its absence might impair neuronal plasticity, contributing to major cognitive deficits of *FOXG1*-haploinsufficient patients [22, 27, 29].

The involvement of a neurodevelopmental transcription factor in the control of mRNA translation is not

novel. It has already been reported in a few cases, including those of Bicoid [60], EMX2 [37], and EN2 [61] homeoproteins. In our case, we found that FOXG1 implication in translation is not limited to *Grin1* only, but it likely is a pervasive phenomenon, affecting hundreds of genes (Figs. 8 and 10), among which a large subset encoding for proteins involved in neuronal metabolism and activity (Additional file 4: Table S2). In a subset of cases, we got robust evidence of physical interaction between mRNAs subject of *Foxg1*-dependent translational control and the FOXG1 protein (Table 1), suggesting that—at least in such cases—the latter may work as a "translation factor". To note, the number of mRNA interactors of FOXG1, 2857, largely exceeded the number of those specifically undergoing FOXG1 control of their translation, 138 + 46 + 47 = 231, pointing to a likely FOXG1 involvement in other aspects of post-transcriptional gene tuning.

Remarkably, albeit our quantification of ribosome engagement and progression was intentionally restricted to the principal isoform of each polypeptide-encoding transcript, as such isoform often shares a large subset of its exon/intron architecture with minor ones, a number of reads originating from the latter were likely misattributed to the former. Next, since different translational gains may apply to distinct isoforms, a change in isoform ratio originating from *Foxg1*-dependent modulation of alternative splicing and/or polyadenylation might have resulted into an artifactual impact of *Foxg1* overexpression on ribosome engagement and progression parameters. To address this issue, we re-analyzed primary totRNA-Seq data from *Foxg1*-OE and control cultures by CASH and ROAR softwares. It turned out that only a minority of presumptive translational targets of FOXG1 regulation underwent *Foxg1*-dependent modulation of splicing and/or polyadenylation patterns (Table 1; Additional file 4: Table S2A, C), therefore allowing us to fix this concern. To note, while running these controls, we detected an additional impact of FOXG1 on two steps of pre-mRNA maturation, i.e., splicing and polyadenylation. We will address these novel aspects of FOXG1 biology in a forthcoming dedicated study.

As said above, we have shown that integrated mining of trap- and total RNA data can provide evidence of FOXG1 control over ribosomes engagement to mRNA, while binning of trap-RNA reads may unveil FOXG1 control of ribosomes progression along it. However, the interpretation of results originating from such approaches deserves caution. This applies firstly to the evaluation of the Δlog2FC parameter. For example, rather than simply reflecting *enhanced translation initiation*, Δlog2FC values above 0 might also alternatively originate from *pronounced ribosome stalling* by the kozak motif. Consistently with this prediction, we found that 8 transcripts out of 183 ones with Δlog2FC > 0 (see Fig. 8B) were also characterized by "average_log2FC(rpi) < 0 and $f_{boi.down}$ z-score > 3". In such cases, FOXG1 could actually *limit* baseline translation (possibly paving the way to subsequent, prompt completion of it, upon the arrival of due inputs). In a symmetrical way, Δlog2FC values below 0 might originate from *extremely fast ribosome progression* along the cds and anticipated detachment from it. Again, consistently with this prediction, we found that 2 transcripts out of 175 ones with Δlog2FC < 0 (see Fig. 8B) were also characterized by "average_log2FC(rpi) > 0 and $f_{boi.up}$ z-score > 3". Here, an increase of FOXG1 levels might elicit an *extremely fast upregulation of translation*, just by relieving ribosomal stalling. Finally, beyond Δlog2FC issues, even the *rpi* (Fig. 10A) has an intrinsically limited predictive power, similar to the corresponding Ribo-seq parameters [62]. In fact, it provides only a static snapshot of presumptive ribosome distribution along mRNA and no direct information about the actual speed at which ribosomes move. For all these reasons, TRAP-seq data mandatorily require to be integrated by experimental investigation of the *actual* rate at which polypeptides of interest are synthesized.

Prompted by these considerations, we challenged results of our total/TRAP-seq analyses, firstly by assessing translation rates of *Sgk1*-and *Homer1*-mRNA, namely two transcripts apparently undergoing FOXG1-driven promotion of ribosome engagement. In both cases, integrated evaluation of puro-PLA results and tot-mRNA dynamics pointed towards an overt translational gain increase evoked by *Foxg1* overexpression (Fig. 9A-C). Remarkably, a comparable increase of SGK1 translation was also evoked upon overexpression of a cytoplasm-confined FOXG1-ERT2 chimera (Fig. 9D-I), ruling out that this phenomenon may trivially reflect an impact of FOXG1 on transcription of translation factor genes. Next, we focused our attention on *Camk2b*- and *Fmr1*-mRNA, namely two transcripts showing 3'-shifted distributions of ^{trap}mRNA-reads upon *Foxg1* overexpression. We measured the temporal decline rate of their translation upon harringtonin blockade of translation initiation, as an index of ribosome progression along their cds. For this purpose, we employed a "puro-PLA run-off" assay, i.e., a novel method we developed to evaluate ribosome advancement speed along specific mRNA-cds (Additional file 1: Figure S3). As expected, this method provided evidence of faster ribosomal progression through *Camk2b*-cds, upon *Foxg1*-OE (Fig. 11A, B, D). In case of *Fmr1*, it conversely pointed to the alternative emergence of a novel ribosomal pausing site, likely evoked by *Foxg1-OE* towards the 3' end of *Fmr1*-cds (Fig. 11A, C, E). Of course, the assays described in Figs. 9 and 11 represent

a small-scale experimental validation of our procedure, which needs to be corroborated by further experimental work. This will be the subject of dedicated follow-up studies.

To note, albeit providing us with only coarse-grained information about ribosome location along mRNA, our reanalysis of "cheap" TRAP-seq data allowed us to identify as many as > 300 genes characterized by a robustly diversified ribosome association to distinctive mRNA regions, dependent on *Foxg1* expression levels (Fig. 10B, C). This suggests that when interested in the control of ribosomal progression rate, mining publicly available TRAP-seq data might be an advisable first approach, prior to moving to more expensive, state-of-art Ribo-seq profiling.

Intriguingly, in a number of cases including *Grin1*, we also found that a large subset of genes characterized by statistically significant Δlog2FC > 0 displayed a robust downregulation of their total-mRNA (118/183) and vice versa for those with Δlog2FC > 0 (117/175) (Fig. 8B, C; Additional file 5: Table S3). In the former case, reminiscent of activity-driven regulation of NPAS4 and ARC [63, 64], the very same effector, FOXG1, might promote a rapid upregulation of the protein, while however limiting the temporal duration of its overexpression. In the latter, FOXG1 could conversely elicit a slow protein upregulation followed by a delayed fast decrease of it. Evolutionarily speaking, multilevel target gene regulation by a single multitask effector is a rare and thermodynamically demanding phenomenon. Such phenomenon could ease the portability/selectability of temporally structured expression programs (in the minutes/hours range). In this way, FOXG1, mainly known as a transcription factor patterning the terminal brain and ruling its histogenesis, could also act as a key multi-scale, temporal modulator of neocortical pyramid plasticity. Interesting per se as well as for its profound neuropathogenic implications, this issue will be specifically investigated in a future, dedicated follow-up study.

Conclusions

In this study, we showed that Foxg1, a transcription factor mastering telencephalic development, stimulates the translation of *Grin1*, encoding for the main subunit of the NMDA receptor. We found that this is associated to increased ribosome engagement to *Grin1*-mRNA and requires physical Foxg1 interaction with EIF4E. Moreover, we discovered that Foxg1 is needed for proper homeostatic response of *Grin1* translation to neuron depolarization.

We further reported that Foxg1 impact on translation is a pervasive phenomenon, affecting hundreds of genes, many of which deeply implicated in neuronal physiology. Depending on cases, Foxg1 may promote or dampen translation, modulating ribosome engagement to mRNA and/or their later progression through cds. Instrumental to these phenomena may be physical Foxg1 interaction with key translation factors EIF4E and EEF1D and target mRNA.

In this way, Foxg1 adds to a small set of transcription factors (including Emx2, En2, and Bcd) which are also implicated in the direct tuning of translation gain. We speculate that orthogonal control of gene transcription and translation exerted by the same polypeptide effector may ease the evolutionary portability of temporally structured expression programs, an issue of paramount relevance to the philogenesis of neuronal excitability dynamics.

Methods

Animal handling

In this study, the following rodent models were employed:

- Wild-type (*wt*) CD1 strain mice (purchased from Envigo Laboratories, Italy);
- Transgenic *Gt(ROSA)26Sor*$^{tm1.1(CAG-EGFP/Rpl10a,-birA)Wtp}$*/J* mice, throughout the text referred to as *Rpl10a*$^{EGFP-Rpl10a/+}$ [40] (founders purchased from Jackson Laboratories, USA, Jax #022386; transgenic line maintained according to Jackson's instructions);
- Transgenic *Mapt*$^{EGFP/+}$ mice [65] (founders purchased from Jackson Laboratories, USA, Jax #004779; transgenic line transferred to CD1 background (> 20 backcrossing generations));
- *wt* Wistar rats (generated at the SISSA animal facility starting from founders purchased from Envigo Laboratories, Italy).

Mutant mouse embryos were obtained by crossing *wt* females to mutant or *wt* males and were staged by timed breeding and vaginal plug inspection. Pregnant dams were killed by cervical dislocation. *Rpl10a*$^{EGFP-Rpl10a/+}$ and *Mapt*$^{EGFP/+}$ mouse embryos were distinguished from their *wt* littermates by UV lamp inspection.

Rat pups were anesthetized with CO2 and sacrificed by decapitation.

Mouse and rat neural tissues were dissected out in sterile ice-cold 1×-phosphate-buffered saline (PBS) supplemented with 0.6% D-glucose (Sigma) under sterile conditions.

Plasmids and lentiviruses

Plasmids employed in this study include:

- LV_pU6-shFoxg1 (Sigma SHCLND-NM_008241, TRCN0000081746); see Figs. 2, 3C, 4B, and 7A.

- LV_pU6-shFoxg1-DPuroR (built by removing the SacII/SacII fragment, including the 5' end portion of puromycin resistance cds and its upstream hPGK-promoter, from "LV_pU6-shFoxg1"; annotated as "LV_pU6-shFoxg1" in Figs. 3A-B, 4A, 8, and 11).
- LV_pU6-shCtrl [14].
- LV_pPgk1-rtTA2S-M2 [66].
- LV_pPgk1-EGFP [5].
- LV_TREt-Foxg1 [67].
- LV_TREt-PLAP [6].
- LV_pPgk1-mCherry [6].
- LV_pPgk1-3xF-wt.mmuFoxg1$^{aa357\text{-}381}$-V5 [built by replacing the AgeI/SalI EGFP-cds fragment of LV_pPgk1-EGFP, by the AgeI/SalI wt.mmuFoxg1$^{aa357\text{-}381}$-V5 module (as detailed in Additional file 6: Table S4)]
- LV_pPgk1-3xF-scr.mmuFoxg1$^{aa357\text{-}381}$-V5 (built by replacing the AgeI/SalI EGFP-cds fragment of LV_pPgk1-EGFP, by the AgeI/XhoI scr.mmuFoxg1$^{aa357\text{-}381}$-V5 module (as detailed in Additional file 6: Table S4))
- LV_TREt-Foxg1-EGFP (built by replacing the SrfI/ApaI fragment of LV_TREt-Foxg1 (including the last 161nt of Foxg1-cds) with the "SrfI-Foxg1(cds-3'term)-EGFP-ApaI" fragment, detailed in Additional file 6: Table S4).
- LV_CMV-Flag-eIF4E (lentivirus of second generation; Addgene plasmid #38239).
- CMV-Flag-GFP (Addgene plasmid #60360).
- CMV-Flag-Gephyrin (a gift from E.Cherubini's Lab).
- LV_CMV-EEF1G-V5 (DNASU Plasmid Repository, HsCD00434091).
- LV_CMV-EEF1D-V5 (DNASU Plasmid Repository, HsCD00444454).
- LV_CMV-PUM1-V5 (DNASU Plasmid Repository, HsCD00438817).
- LVrc_TREt-pl-BGHpA (built by replacing the "pPgk1-EGFP-WPRE" fragment of "LV_pPgk1-EGFP" b y a "TREt-polylinker-BGHpA" stuffer, in a 3'LTR-to-5'LTR orientation (as detailed in Additional file 6: Table S4))
- LVrc_TREt-rnoGrin1-203*.full (built by introducing a STOP codon and a polylinker after codon 30 of *rnoGrin1-203* cDNA and transferring the resulting "rnoGrin1-203*.full" fragment (detailed in Additional file 6: Table S4) into $^{filled\text{-}in}$XhoI/XbaI-cut "LVrc_TREt-pl-BGHpA" vector).
- LVrc_TREt-rnoGrin1-203*.d1 (5'utr deletion) (built by replacing the BstBI/PmeI fragment of "LVrc_TREt_rnoGrin1-203*.full" with the synthetic "BstBI-GAGCTC-(rnoGrin1-203*:1-30aa)-STOP-PmeI" module).
- LVrc_TREt-rnoGrin1-203*.d2 (cds1 deletion) (built by removing the AccIII/AccIII fragment from "LVrc_TREt_rnoGrin1-203*.full").
- LVrc_TREt-rnoGrin1-203*.d3 (cds2-3'utr deletion) (built by removing the KpnI/KpnI fragment from "LVrc_TREt_rnoGrin1-203*.full").
- LVrc_TREt-rnoGrin1-203*.d4 (3'utr deletion) (built by removing the PshAI/BamHI fragment from "LVrc_TREt_rnoGrin1-203*.full").
- LVrc_TREt-rnoGrin1-203*.d5 (cds3 deletion) (built by removing the PmeI/PshAI fragment from "LVrc_TREt-rnoGrin1-203*.full").
- LV_TREt-Foxg1.ert2.flag3.v5 (detailed in Additional file 6: Table S4) (provided on a commercial basis by Gene Universal Inc.).

Starting from a subset of these plasmids, self-inactivating lentiviral vectors (LV) were generated and titrated as previously described [5].

Primary neural cell cultures

Cortical (or tectal) tissue from E16.5 mice or hippocampal tissue from P1 mouse pups were chopped to small pieces for 5 min, in the smallest volume of ice-cold 1×PBS—0,6% D-glucose—5mg/ml DNaseI (Roche #10104159001) solution. After chemical digestion in 2.5×trypsin (Gibco #15400054)—2 mg/ml DNaseI (Roche) for 5 min and trypsin inhibition with DMEM-glutaMAX (Gibco)—10% FBS (Euroclone)—1×Pen-Strep (Invitrogen), cells were spinned down and transferred to differentiative medium (Neurobasal-A (Gibco), 1×Glutamax (Gibco), 1×B27 supplement (Invitrogen), 25 µM L-glutamate (Sigma), 25 µM β-Mercaptoethanol (Gibco), 2% FBS (Euroclone), 1×Pen/Strept (Invitrogen), and 10 pg/ml fungizone (Invitrogen)). Cells were counted and plated as follows:

(a) in case of RNA profiling (totalRNA-, TRAP-, and RIP-qRTPCR assays) and western blot experiments, cells were plated onto 0.1 mg/ml poly-L-Lysine (Sigma #P2636) pre-treated 12-multiwell plates (Falcon) at 8×10^5 cells/well in 0.6–0.8 ml differentiative medium;

(b) in case of immunofluorescence and PLA assays, cells were plated onto 0.1 mg/ml poly-L-lysine pre-treated 12 mmØ glass coverslips in 24-multiwell plates (Falcon) at 1×10^5 cells/well in 0.6–0.8 ml differentiative medium.

(c) in case of live imaging, cells were plated onto 0.1 mg/ml poly-L-lysine pre-treated 35 mmØ glass dishes (Ibidi), at 0.8×10^5 cells/dish, in 2 ml differentiative medium/dish.

In general, when required and as indicated in each figure: (a) lentiviral infection was done at DIV1-3; (b) TetON-regulated transgenes were activated by 2 µg/ml doxycycline (Clontech #631311) administration; and (c) 10 µM cytosine β-D-arabinofuranoside (AraC; Sigma #C6645) was acutely added to the medium at DIV1. Cells were kept in culture for 8 days.

Live imaging of primary hippocampal cell culture

Hippocampal cultures, set as described above and engineered as in figure legend, were analyzed at DIV8 as follows. Cultures were supplemented by 50 nM Mitotracker dye (Life Technologies #M7512) for 30 min, medium was replaced by PBS, and confocal images were immediately acquired. Live fluorescent imaging was done with a confocal microscope (NIKON A1R) equipped with 488 nm and 594 nm laser excitation light and a 60×oil immersion objective (N.A. 1.40), keeping samples at 37 °C, 5% CO2, and 95% humidity.

HEK293T cell cultures

HEK293T cells were used for lentivirus production, lentivirus titration (Brancaccio et al. 2010), as well as to evaluate protein–protein interactions via co-immunoprecipitation (co-IP) and proximity ligation assay (PLA). HEK293T cells were cultured in DMEM-glutaMAX—10% FBS—1×Pen-Strep, on 6-multiwell plates at 1.2×10^6 cells/well (for co-IP assays) or on 0.1 mg/ml poly-L-lysine pre-treated 12 mmØ glass coverslips in 24-multiwell plates at 3×10^5 cells/well (for PLA assays). In all cases, cells were transfected by LipoD293 (SignaGen laboratories #SL100668) at DIV1, according to manufacturer's instructions. Cells were further kept in culture for 3 and 2 days, for co-IP and PLA assays, respectively, and finally analyzed.

Immunofluorescence assays

Neural cell cultures were fixed by ice-cold 4% PFA for 15–20 min and washed three times in 1×PBS. Samples were subsequently treated with blocking mix (1×PBS; 10% FBS; 1mg/ml BSA; 0.1% Triton X-100) for at least 1 h at room temperature (RT). After that, incubation with primary antibodies was performed in blocking mix, overnight at 4°C. The day after, samples were washed three times in 1×PBS—0.1% Triton X-100 for 5 min and then incubated with secondary antibodies in blocking mix, for 2 h at RT. Samples were finally washed three times in 1×PBS—0.1% Triton X-100 for 5 min, and subsequently counterstained with DAPI (4', 6'-diamidino-2-phenylindole) and mounted in Vectashield Mounting Medium (Vector).

The following primary antibodies were used:

- Anti-Flag, mouse monoclonal, clone M2, Sigma #F1804, 1:1000;
- Anti-FOXG1 ChIP-grade, rabbit polyclonal, Abcam #ab18259, 1:500 [Fig. 9E, S4B, S5B];
- Anti-FOXG1, rabbit polyclonal, gift from G.Corte, 1:200) [Fig. 1A, S5A];
- Anti-NEUN, guinea pig polyclonal, affinity purified, Merck #ABN90P, 1:800.
- Anti-PSD95, mouse monoclonal, clone 6G6-1C9, Abcam #ab2723, 1:500;
- Anti-Puromycin, mouse monoclonal, clone 12D10, Millipore #MABE343, 1:4000;
- Anti-SMI312, mouse monoclonal, Abcam #ab24574, 1:1000;
- Anti-TUBB3, mouse monoclonal, clone Tuj1, Covance #MMS-435P, 1:1000;
- Anti-V5, mouse monoclonal, clone SV5-Pk1, Abcam #ab27671, 1:800.

Secondary antibodies were conjugates of Alexa Fluor 488 and Alexa Fluor 594 (Invitrogen, 1:600).

Proximity ligation assays (PLAs), puro-PLAs, puro-PLA-run-off assays

PLA assays were performed according to manufacturer's instructions (Duolink™ PLA Technology, Sigma). Briefly, cells were fixed for 15–20 min in ice-cold 4% PFA, washed three times in 1×PBS, permeabilized in 1×PBS×0.1% Triton X-100 for 1h at RT, blocked for 1 h at 37°C in Duolink blocking buffer and incubated for 3 h/overnight at RT with mouse and rabbit primary antibodies (as indicated in the corresponding Figures). Afterwards, samples were washed three times for 5 min in Duolink buffer A and then incubated for 1 h at 37°C with Duolink anti-mouse MINUS and anti-rabbit PLUS probes, both co-diluted 1:5 in Duolink antibody dilution buffer. Next, samples were washed three times for 5 min in buffer A, incubated for 30 min at 37°C in Duolink ligase diluted 1:40 in 1×ligation buffer, washed again three times in buffer A, and incubated for 100 min at 37°C in Duolink polymerase diluted 1:80 in 1×green or red amplification buffer. Finally, samples were washed two times for 10 min in Duolink buffer B and 1 time in 1:100 buffer B for 1 min and mounted in Duolink mounting medium with DAPI. Then, by 48 h, confocal images were acquired.

Puro-PLA samples [68] were prepared as indicated in the corresponding figures and schematized in Additional file 1: Figure S3. Briefly, cortico-cerebral cells were pulsed for 5 min with 3 µM puromycin (Sigma #P8833) or with 1×PBS (negative control) and, immediately afterwards,

fixed in ice-cold 4% PFA for 15 min. Then, they were processed by standard PLA, as above.

Puro-PLA-run-off DIV8 samples were prepared as indicated in the corresponding figures. In particular, before terminal puromycin labeling, cells were cumulatively exposed to 2 µg/ml harringtonine (Abcam #ab141941) for 20' or (20 + x)' depending on the "T0'" or the "Tx'" branch of the protocol and 208 µM emetine (Sigma #E2375) for 20 min. Finally, during the last 5' of harringtonin/emetin treatment, unfinished polypeptides were labeled via further medium supplementation by 10 µg/ml puromycin. Immediately afterwards, samples were fixed in ice-cold 4% PFA for 15 min and processed for standard PLA, as above.

The following primary antibodies were used:

- Anti-CAMK2B, rabbit polyclonal, GeneTex #GTX133072, 1:500;
- Anti-EEF1D, mouse monoclonal, clone 3B1B11, Proteintech #60085-1-Ig, 1:200;
- Anti-EIF4E, mouse monoclonal, clone 5D11, Thermofisher #MA1-089, 1:100;
- Anti-Flag, mouse monoclonal, clone M2, Sigma #F1804, 1:1000.
- Anti-FMR1, rabbit monoclonal, Huabio #ET1703-70, 1:500;
- Anti-FOXG1, rabbit polyclonal, ChIP-grade, Abcam #ab18259, 1:500;
- Anti-GRIN1 COOH-term, rabbit monoclonal, clone EPR2481(2), Abcam #ab109182, 1:500;
- Anti-GRIN1 NH2-term, rabbit polyclonal, Alomone #AGC-001, 1:500;
- Anti-HOMER1, rabbit polyclonal, GeneTex #GTX103278, 1:300;
- Anti-NMT1, rabbit polyclonal, GeneTex #GTX130852, 1:500;
- Anti-puromycin, mouse monoclonal, clone 12D10, Millipore #MABE343, 1:1000;
- Anti-SGK1, rabbit polyclonal, GeneTex #GTX54726, 1:200;
- Anti-V5, mouse monoclonal, clone SV5-Pk1, Abcam #ab27671, 1:1000.

Neuronal stimulation assays

Cortico-cerebral cultures were set up as described above (to see "Primary neural cell cultures") and as detailed in Fig. 7. Specifically, their terminal DIV8 manipulation was as follows. "K5" samples were pulsed with 55 mM KCl-supplemented medium for 5 min. "K10-noK25" samples were firstly pulsed with 55 mM KCl-supplemented medium for 10 min and then transferred to a conditioned medium, taken from unstimulated sister cultures, for 25 min. "Ctr" samples were kept in standard, not KCl-supplemented medium. Next, "K5", "K10-noK25," and "Ctr" cells were all pulsed by 3 µM puromycin for 5 min and, immediately afterwards, fixed in ice-cold 4% PFA for 15 min.

Photography and image analysis

Basic immunofluorescence

αFoxg1-, αTubb3-, αPSd95-, αSmi312-, and αPuro-immunoprofiled cells were photographed by a Nikon C1 confocal system equipped with 40×oil objective (Figs. 1A–F and 3B). Photos were collected as 3 µm Z-stacks (step = 0.3 µm). Upon Z-stack flattening (max version), pictures were imported into Adobe Photoshop CS6, for subsequent processing. αFlag- and αHA-immunoprofiled cells were photographed by a Nikon Eclipse TI microscope, equipped with a 40×objective through the Hamamatsu 1394 ORCA-285 camera (Fig. 4B). Collected as 1024×1024 (case Fig. 3B) and 1344×1024 pixel images (case Fig. 4B), photos were imported in Volocity 6.5.1 for analysis (Figs. 3B and 4B). Here, for each individual neuron, an ROI was outlined by an operator blinded of sample identity and background-subtracted, average αFlag, and αHA, non-nuclear signals, and total-cell αPuro signal were collected.

PLA analysis

PLA-profiled cells were photographed by a Nikon C1 confocal system equipped with 40×oil objective (Figs. 3A, 6, 7, 9, and 11; Additional file 1: Figure S2A). Photos were collected as 2 µm Z-stacks (step = 1µm) and 3 µm Z-stacks (step = 1µm) of 1024×1024 pixel images, for Additional file 1: Figure S2A and Figs. 3A, 5, 7, 9, and 11, respectively. All primary images were generally analyzed with Volocity 6.5.1 software (here, positive spots were 3D clusters including ≥ 1 voxels, each voxel corresponding to 0.1 μm^3 and displaying a signal above 90 background standard deviations; for cumulative PLA signal calculation, only voxels above this threshold were taken into account). Limited to Fig. 5A (b), files originating from flattened Z-stacks (max version) were imported into Adobe Photoshop CS6 and 2D-spots counting was performed manually by an operator blind of sample identity. When appropriate (Figs. 3A and 5A), spot counting and/or cumulative signal evaluation was restricted to specific cell compartments (highlighted in gray, in idealized neuron silhouettes).

Common

Results of numerical image analysis were imported into Microsoft Excel for subsequent processing. Finally, representative photos were edited for figure preparation by ImageJ-Fiji and Adobe Photoshop CS6 softwares.

Total RNA extraction

Total RNA was extracted from cells (Fig. 2D, E) using TRIzol Reagent (Thermofisher) according to the manufacturer's instructions, with minor modifications. Briefly, for each biological replicate, a pellet including 300,000–800,000 cells was dissolved in 250–500 µl of Trizol. RNA was precipitated using isopropanol and GlycoBlue (Ambion) overnight at −80°C. After two washes with 75% ethanol, the RNA was resuspended in 20 µl sterile nuclease-free deionized water. Agarose gel electrophoresis and spectrophotometric measurements (NanoDrop ND-1000) were employed to estimate its concentration, quality, and purity.

Translating ribosome affinity purification (TRAP) assay: RNA preparation

The TRAP assay was performed as previously described [52, 69] with minor modifications. For each TRAP reaction, 10 µg of anti-GFP antibody, purchased from the Monoclonal Antibody Core Facility at the Memorial Sloan-Kettering Cancer Center (purified form of HtzGFP-19C8), was covalently bound to 1 mg magnetic epoxy beads (Dynabeads Antibody Coupling kit, Life Technologies #14311D), according to manufacturer's protocols, followed by BSA treatment to reduce non-specific binding. Antibody-coupled beads were resuspended at the concentration of 1 mg/100µl. Cortico-cerebral cells, derived from *Rpl10a*$^{EGFP-Rpl10a/+}$ embryos, were set up as described above (see "Primary neural cell cultures") and as detailed in Fig. 2A. At DIV8, cells were treated by supplementing the medium with 0.1mg/ml cycloheximide (CHX; Sigma #C7698) at 37°C for 15 min. Then, cells were washed two times with ice-cold 1×PBS containing 0.1mg/ml CHX; 75 µl ice-cold lysis buffer (see below) was added to each cell-containing well (12-multiwell plate) for 10 min on ice. Afterwards, cells were scraped and lysed by vigorously pipetting them up and down without creating bubbles. The lysate derived from two wells (about 1.6×10^6 cells; corresponding to one biological replicate) was pooled. Upon addition to each replicate sample of 1/9 volume of 300 mM 1,2-dihexanoyl-sn-glycero-3-phosphocholine (DHPC, Avanti Polar Lipids #850305), such sample was firstly centrifuged at 2000*g* for 10 min at 4°C. The supernatant was harvested and re-centrifuged, at 20,000*g* for 10 min at 4°C. The resulting supernatant (about 150 µl) was incubated with 100 µl antibody-coupled beads for 1 h at 4°C on a rotating wheel at 10 rpm. After incubation, beads were collected with a magnet: the immunoprecipitated component (TRAP-IP) bound to beads was washed four times with 1 ml of ice-cold high-salt buffer (see below); the supernatant component (TRAP-SN) of each sample was stored on ice. (Lysis buffer: 20 mM HEPES (Ambion), 150 mM KCl (Ambion), 10 mM MgCl2 (Ambion), 1%(vol/vol) NP-40 (Thermo Fisher Scientific), 1×EDTA-free protease inhibitors (Roche), 0.5 mM DTT (Invitrogen), 0.1 mg/ml cycloheximide, 10 µl/ml rRNasin (Promega), and 10 µl/ml Superasin (Applied Biosystems). High-salt buffer: 20 mM HEPES, 350 mM KCl, 10 mM MgCl2, 1%(vol/vol) NP-40, 1×EDTA-free protease inhibitors, 0.5mM DTT, 0.1 mg/ml cycloheximide). For each sample, RNA of TRAP-SN and TRAP-IP fractions were extracted with Trizol® LS reagent (Thermofisher) according to manufacturer's instructions, with minor modifications. The extraction procedure was repeated to improve RNA sample purity. RNA was finally precipitated using NaOAc, isopropanol, and GlycoBlue overnight at −80°C, according to standard protocols. After two washes with 75% ethanol, the RNA was resuspended in 10 µl sterile nuclease-free deionized water. Agarose gel electrophoresis and spectrophotometric measurements (NanoDrop ND-1000) were employed to estimate quantity, quality, and purity of the resulting preparation.

RNA immunoprecipitation (RIP) assay: RNA preparation

Cortico-cerebral cells were set up as described above (see "Primary neural cell cultures") and as detailed in Fig. 6. For each RIP reaction, 10 µl of protein A/G Dynabeads (Thermofisher #492024) were coupled with 10 µg of anti-protein of interest (POI; anti-FOXG1 ChIP-grade, rabbit polyclonal, Abcam #ab18259; anti-GFP, rabbit polyclonal, Abcam #ab290), or 10 µg of rabbit IgG (Millipore #12370) as control, according to manufacturer's protocols. Pre-clearing beads were prepared omitting antibody coupling. DIV8 cells were washed once with ice-cold 1×PBS; 75 µl ice-cold lysis buffer (see below) was added to each cell-containing well (12-multiwell plate) for 10 min on ice. Afterwards, the cells were scraped and lysed by vigorously pipetting them up and down without creating bubbles. The lysate derived from 10 wells (about 8×10^6 cells; to be employed for one set of paired anti-POI/IgG assays) was pooled, pipetted up and down, and kept 10 min on ice. Pipetting and incubation on ice were repeated. Next, each sample was centrifuged at 2000*g* for 10 min at 4°C. Then, the supernatant was re-centrifuged, at 16,000*g* for 10 min at 4°C. The resulting supernatant was incubated with pre-clearing beads (pre-equilibrated in lysis buffer, see below) for 30 min at 4°C on a rotating wheel, at 10rpm. Then, the pre-clearing beads were removed with a magnet, and the supernatant was incubated with antibody-coupled beads (pre-equilibrated in lysis buffer), overnight at 4°C on a rotating wheel, at 10 rpm; 10% of supernatant (Input, RIP-IN) was stored at −80°C. The day after, the beads were collected with a magnet and the immunoprecipitated material bound to beads was harvested by washing them five times

with 0.5 ml of ice-cold high-salt buffer. (Lysis buffer: 25 mM TRIS-HCl, 150 mM KCl (Ambion), 10 mM MgCl2 (Ambion), 1%(vol/vol) NP-40 (Thermo Fisher Scientific), 1×EDTA-free protease inhibitors (Roche), 0.5 mM DTT (Invitrogen), 10 µl/ml rRNasin (Promega), and 10 µl/ml Superasin (Applied Biosystems). High-salt buffer: 25 mM TRIS-HCl, 350 mM KCl (Ambion), 10 mM MgCl2 (Ambion), 1% (vol/vol) NP-40 (Thermo Fisher Scientific), 1×EDTA-free protease inhibitors (Roche), and 0.5 mM DTT (Invitrogen)). For each sample, immunoprecipitated RNA (RIP-IP) and input (RIP-IN) were extracted with Trizol® LS reagent according to manufacturer's instructions, with minor modifications. The extraction procedure was repeated to improve RNA sample purity. RNA was precipitated using isopropanol and GlycoBlue overnight at −80°C, according to standard protocols. After two washes with 75% ethanol, the RNA was resuspended in 10 µl sterile nuclease-free deionized water. Agarose gel electrophoresis and spectrophotometric measurements (NanoDrop ND-1000) were employed to estimate quantity, quality, and purity of the resulting RNA.

RNA quantitation: DNase treatment, reverse transcription, and real-time quantitative PCR

DNA contaminants were removed from total RNA, TRAP-SN, RIP-IN, and RIP-IP samples by treating them with TURBO™ DNase (2U/µl) (Ambion) for 1 h at 37°C, following manufacturer's instructions. cDNA was produced via reverse transcription (RT) of the resulting preparations by SuperscriptIII™ (Invitrogen), primed by random hexamers, according to manufacturer's instructions. For RT reactions, the following aliquots of RNA preparations were used: 1/10 TRAP-IP, 1/10 (DNA-free) TRAP-SN, 1/6 (DNA-free) IP- and IN-RIP, and 0.5 µg (DNA-free) total RNA. Following SuperscriptIII™ thermo-inactivation, the RT reaction (20 µl) was diluted 1:3 (in case of TRAP samples) or 1:5 (in case of RIP and total RNA samples), and 1–2 µl of the resulting cDNA solution was used as substrate of any subsequent quantitative PCR (qPCR) reaction. Limited to intronless amplicons and/or TRAP-IP, RIP-IN, and RIP-IP samples, negative control PCRs were run on RT(-) RNA preparations. qPCR reactions were performed by the SsoAdvanced SYBR Green Supermix™ platform (Biorad), according to manufacturer's instructions, on a CFX Bio-Rad thermocycler.

For each transcript under examination and each sample (i.e., biological replicate), cDNA was qPCR-analyzed in technical triplicate and results averaged. In case of total RNA and TRAP-IP and TRAP-SN samples, mRNA levels were normalized against *Rpl10a*-mRNA [70]. In addition, in case of TRAP samples, IP/SN ratios were further calculated per each sample, as indices of mRNA engagement to holoribosomes. In case of RIP samples, IP values were straightly normalized against IN values. Final results were averaged and the corresponding sems calculated using Excel software.

The following oligonucleotides have been employed in this study:

Psd95/F: GCCGTGGCAGCCCTGAAGAACACA
Psd95/R: GCTGCTATGACTGATCTCATTGTC CAGG
Foxg1(cds)/F: GACAAGAAGAACGGCAAGTAC GAGAAGC
Foxg1(cds)/R: GAACTCATAGATGCCATTGAG CGTCAGG
Foxg1(*5utr*)/F: TAGAAGCTGAAGAGGAGGTGG AGTGC
Foxg1(*5utr*)/R: CAGACCCAAACAGTCCCGAAA TAAAGC
Gria1/F: TCCATGTGATCGAAATGAAGCATG ATGGAATCC
Gria1/R: CGATGTAGGTTCTATTCTGGACGC TTGAGTTG
pan-Grin1/F: CGAGGATACCAGATGTCCACC AGACTAAAGA
pan-Grin1/R: CTTGACAGGGTCACCATTGAC TGTGAACT
ex20-Grin1/F: CCGTGAACGTGTGGAGGAAGA ACCT
ex20-Grin1/R: GTGTCTTTGGAGGACCTACGT CTCTTG
Grid1/F: AAGGACTGACTCTCAAAGTGGTGA CTGTCTT
Grid1/R: CCTTAGCCAGTGCATCCAGCACAT CTATG
Gabra1/F: AAACCAGTATGACCTTCTTGGACA AACAGTTGAC
Gabra1/R: GTGGAAGTGAGTCGTCATAACCAC ATATTCTC
Slc17a6/F: TTTTGCTGGAAAATCCCTCGGACA GATCTACA
Slc17a6/R: CTTACCGTCCTCTGTCAGCTCGAT GG
Bdnf2c/F: CTTTGGGAAATGCAAGTGTTTATC ACCAGGAT
Bdnf4/F: CTGCCTTGATGTTTACTTTGACAA GTAGTGACTG
Bdnf(2c,4)/R: GCCTTCATGCAACCGAAGTAT GAAATAACCATAG
Rpl10a/F: CAGCAGCACTGTGATGAAGCCAAGG
Rpl10a/R: GGGATCTGCTTAATCAGAGACTCA GAGG

F-rnoGrin1-H/F: ACCTCCACCCTGGCCTCC AGCTT
F-rnoGrin1-H/R: GGGATAGCCAGCGTAATC TGGAACATC
rnoGrin1.d/F1: AGATCGCCCTCGACTTCGAAG AGC
rnoGrin1.d/F2: GTCGCACTCGCGCAACCC AGAG
rnoGrin1.d/F3: CCCAAGATCGTCAACATCGGC TGAGT
rnoGrin1.d/F4: CTGGCCGTGTGGAATTCAATG AGGATG
rnoGrin1.d/F5: TGCAGGATAGAAAGAGTGGTA GAGCAGA
rnoGrin1.d/F6: CAGTGGTGATGCCTAAAGGAA TGTCAG
rnoGrin1.d/R1: CTCAGCACCGCCTCGAGTCCG
rnoGrin1.d/R2: ACTTCTGTGAAGCCTCAAACT CCAGCA
rnoGrin1.d/R3: TCCTCCCTCTCAATAGCG CGTCG
rnoGrin1.d/R4: TGTGGGTGACAGAAGTGGCGT TGAG
rnoGrin1.d/R5: GGGCAAACAACAGATGGCTGG CAACT

NB. rnoGrin1.d oligos employed for assays referred to by Fig. 6B were associated as follows:

- d0/d1 assay: *rnoGrin1.d*/F1, *rnoGrin1.d*/F2, *rnoGrin1.d*/R1;
- d0/d2 assay: *rnoGrin1.d*/F3, *rnoGrin1.d*/R2, *rnoGrin1.d*/R4;
- d0/d3 assay: *rnoGrin1.d*/F4, *rnoGrin1.d*/F6, *rnoGrin1.d*/R5;
- d0/d4 assay: *rnoGrin1.d*/F5, *rnoGrin1.d*/F6, *rnoGrin1.d*/R5;
- d0/d5 assay: *rnoGrin1.d*/F3, *rnoGrin1.d*/R3, *rnoGrin1.d*/R4.

TRAP-seq profiling

Produced as described in the "Translating ribosome affinity purification (TRAP) assay: RNA preparation" section, TRAP-IP samples were sequenced by IGA Technology Services Srl. Libraries were produced using retrotranscribed cDNA previously amplified by Ovation Ultralow Library System V2 (NuGEN Technologies, Inc.). Library size and integrity were assessed using the Agilent Bioanalyzer (Santa Clara, CA) or Caliper GX (PerkinElmer, MA) apparatus. Sequencing was performed by Illumina HiSeq 2500 (Illumina, San Diego, CA); 20M paired-end reads (2×125 nt) per biological replicate were generated (as elsewhere, biological replicates are independently cultured and engineered preparations, originating from a common cell pool); 3 *Foxg1*-OE and 4 Ctr replicate samples were profiled. Quality control of the sequenced reads was performed by a commercial operator (Sequentia, Barcelona, Spain) with the FASTQC v0.11.5 software, then low-quality bases and adapters were removed with the software BBDuk version 35.85, setting a minimum base quality of 30 and a minimum read length of 35 bp. So-filtered high-quality reads were used in the following analyses.

Ribosome engagement analysis

Transcripts whose ribosome engagement was affected by *Foxg1* overexpression were identified as follows. First, *Mus musculus* mRNA sequences (GRCm38.p6 reference genome version) were retrieved by Ensembl Biomart [71], selecting the principal isoform of each gene according to APPRIS annotations [45] (if more transcripts were indexed at the highest level, then the longest one was selected). The resulting reference transcriptome included 22,442 transcripts. On this transcriptome, total RNA-seq FASTQ reads [17] as well as TRAP-seq FASTQ reads, originating from sister primary neural cultures, were mapped using Bowtie2 [72] (in "very-sensitive-local" configuration). Finally, the number of reads mapped to each transcript was computed by means of featureCounts [73] (with "primaryOnly = TRUE" and "minMQS = 10" settings).

Next, for both total RNA-seq and TRAP-seq assays, differential gene expression analysis was performed using the R package DESeq2 software [46]. Then, for each gene, the difference between log2FC(trapRNAseq) and log2FC(totalRNAseq) (named Δlog2FC) was primarily calculated, as an index of *Foxg1*-OE impact on mRNA engagement to ribosomes. Moreover, statistical significance of Δlog2FC values was evaluated with Python package Ribodiff software (default parameters) [47]. Finally, genes were filtered out if not satisfying "$p$adj < 0.1" conditions, as well as if not reaching the "baseMean" DESeq2 value of 200 in case of both RNA-seq and TRAP-seq profiling (Artimagnella and Mallamaci, doi: temporarily restricted).

Ribosome progression analysis

This analysis was performed, taking advantage of the reference transcriptome generated for ribosome engagement analysis. TRAP-seq FASTQ reads were mapped on it using Bowtie2 (in "very-sensitive-local" configuration) and those falling within the cds further taken into account. Hence, for each transcript, the cds was divided in 125-nt bins and the number of reads mapping to each bin was computed by featureCounts (with

"allowMultiOverlap = TRUE", "primaryOnly = TRUE", and "minMQS = 10" settings). Transcripts with < 4 reads/bin in at least one sample out of seven were filtered out. Then, for each bin/bin boundary, the ribosomal progression index (RPI) was calculated, as the ratio between the numbers of reads mapping downstream and upstream of it (to avoid potential infinites, numerator and denominator were increased by 1). The RPI of the last bin (3' end) of all transcripts was discarded. Transcripts including a single cds-bin were not considered. Finally, for each bin of the 5040 transcripts analyzed which passed all the filters, the fold change (FC), i.e., the ratio among average RPI values peculiar to *Foxg1*-OE and *Ctr* groups, was calculated, and its statistical significance evaluated by *t*-test.

Next, for each transcript, boundaries with log2FC(RPI) ≥ 1 and $p < 0.05$ were annotated as "boundaries of interest, up" (boiups) and those with log2FC(rpi) ≤ -1 and $p < 0.05$ as "boundaries of interest, down" (boidowns). Then, boiups and boidowns frequencies were evaluated over the full cds (*f*boi.up and *f*boi.down, respectively). Finally, 34, (4 + 3)-type permutations of samples-set were built and the above analysis was performed for each of them in order to filter out potential false positive gene. Therefore, for each gene, *f*boi.up and the *f*boi.down z-scores were calculated and genes with z-scores < 3 were filtered out (Artimagnella and Mallamaci, doi: temporarily restricted).

Gene Ontology analysis

Gene Ontology analysis (GO) was performed with R package gProfiler2 software [74] (with "exclude_iea = T, user_threshold = 0.1, sources = GO and correction_method = fdr" settings).

In the case of "Ribosome engagement analysis" genes, the input was the set of 358 "differentially engaged transcripts" (with *p*adj < 0.1), while the background (custom_bg argument) included the 5122 transcripts with DESeq2 "baseMean" ≥ 200 (referring to both RNA-seq and TRAP-seq data). FDR was set at 0.1.

In case of "Ribosome progression analysis" genes, the input was the set of 328 genes with *f*boi.up-z-score ≥ 3 or *f*boi.down-z-score ≥ 3, while the background (custom_bg argument) included the 5040 genes which passed all the "counting" filters listed above (Artimagnella and Mallamaci, doi: temporarily restricted). FDR was set at 0.2.

Splicing and polyadenylation analyses

Both analyses were executed on totRNA samples from *Foxg1*-OE and control neocortical cultures [18] by a commercial operator (Sequentia, Barcelona, Spain).

In the case of splicing analysis, CASH software [48] was used. Genes with $-0.1 \geq \Delta psi \geq 0.1$ and fdr < 0.05 were considered significant (here, Δpsi is the difference in percentage of "spliced-in transcripts" between *Foxg1*-OE and control samples).

In the case of polyadenylation analysis, ROAR software [49] was used. Genes with $1/1.2 \geq r \geq 1.2$ and *p*adj < 0.05 were considered significant (here, being the m/M the ratio between the shortest and the longest polyA isoform, *r* is the ratio between *Foxg1*-OE and control m/M parameters).

RIP-seq profiling

Produced as described in "RNA immunoprecipitation (RIP) assay: RNA preparation" section, RIP samples were sequenced by IGA Technology Services Srl. Libraries were produced using retrotranscribed cDNA previously amplified by Ovation Ultralow Library System V2 (NuGEN Technologies, Inc.). Library size and integrity were assessed using the Agilent Bioanalyzer (Santa Clara, CA) or Caliper GX (PerkinElmer, MA) apparatus. Sequencing was performed by Illumina HiSeq 2500 (Illumina, San Diego, CA); 10 M paired-end reads (2 × 125nt) per replicate were generated; 3 anti-Foxg1 and 3 IgG-Ctr paired samples were profiled. Quality control of the sequenced reads was performed by a commercial operator (Sequentia, Barcelona, Spain). Reads were processed with the FASTQC v0.11.5 software, then low-quality bases and adapters were removed with the software BBDuk version 35.85, setting a minimum base quality of 30 and a minimum read length of 35 bp. So-filtered high-quality reads were used in the following analyses.

RIP-seq analysis and identification of FOXG1-protein-interacting transcripts with Foxg1-sensitive ribosomal engagement and progression rates

Foxg1 protein-bound transcripts were identified as follows (steps 1–3 executed by Sequentia, Barcelona, Spain).

First, a reference transcriptome was generated. The web-based tool Biomart [71] was used to extract GeneIDs, TranscriptIDs, cDNA sequences, APPRIS annotations [45], and transcript support levels (TSLs) of mouse genome GRCm38.p6. To select a unique representative transcript per gene, these rules were sequentially implemented: (1) the transcript with the highest APPRIS annotation level was chosen; (2) if multiple transcripts with the same annotation level were available, the transcript with the highest TSL was chosen; (3) if more than one transcript had the same TSL, one of them was randomly selected; and (4) if a gene had no transcripts with either an APPRIS annotation or a TSL, one transcript was also randomly chosen. The final reference transcriptome consisted of 55,647 unique transcripts.

Second, prior to mapping the reads to transcripts, the reference transcriptome was indexed with STAR (version

2.7.9a), using the genomeGenerate function. The parameter "genomeChrBinNbits" was set according to the formula:

$$min(18, log2(max(GenomeLength/AmountOfReferences, ReadLength)))$$

RIP-seq reads were mapped in local alignment mode, with maximum intron size set to 1, so that the resulting BAM files did not actually include reads mapped on introns.

Third, Foxg1 protein/mRNA interaction peaks were identified by SICER2 (version 1.0.2) [75]. The SICER2/sicer/lib/GenomeData.py file was manually edited in the SICER2 repository, to include a list of our reference transcriptome transcripts IDs, and a Python dictionary that maps these IDs to their lengths. Moreover, SICER was run setting its parameters as follows: "fragment_size = median read length", "redundancy_threshold = 1", "window_size = 200", "gap_size = 200", and "effective_genome_fraction = 1". In this way, 8352, 8851, and 7120 peak islands with fdr < 0.1 were identified in samples 1, 2, and 3, respectively.

Fourth, peak islands were filtered out if not satisfying "aFoxg1/IgG_enrichment ≥ 2" and "fdr < 0.05". Next, transcripts sharing ≥ 1 peak island in ≥ 2 out of 3 biological replicates were considered as interacting with the Foxg1 protein. A total of 2857 transcripts satisfied this requirement.

Fifth, to estimate the magnitude of the geneset undergoing direct Foxg1 regulation of translation, these 2857 transcripts were intersected with the 358 and 328 ones resulting from our "Ribosome engagement analysis" and "Ribosome progression analysis" pipelines, respectively.

z.

Co-immunoprecipitation (co-IP) assay

HEK293T cell lines were cultured and transfected as described in "HEK293T cell cultures" section and as detailed in Additional file 1: Figure S3B. After 3 days, cells were washed in 1 × PBS and lysed with 500 µl of CHAPS buffer, supplemented with 1 × protease inhibitors (Roche). Next, lysates were processed for co-IP analysis by the FLAG Immunoprecipitation Kit (Sigma), according to manufacturer's instructions. Specifically, total cell lysates were centrifuged at 12,000*g* for 10 min at 4°C to remove debris. For each sample, the 4% of supernatant was saved as input (IN). The remaining part was incubated with anti-Flag-conjugated resin for 3h at 4 °C, on a rotating wheel. Next, the immuno-precipitated resin (IP) was resuspended and washed four times in 1 × wash buffer. Finally, IP and IN samples were denatured at 95 °C for 5 min in 1 × sample buffer (supplemented with 0.5% β-Mercaptoethanol), prior to subsequent western blot analysis.

Protein degradation assay

Cortico-cerebral cells were set up as described above (see "Primary neural cell cultures") and as detailed in Fig. 3C. At DIV8, cells were treated with 50 µg/ml cycloheximide (CHX). Cells were analyzed at four different time points, 0, 3, 6, 10, and 14 h after CHX administration. For each point, samples were lysed in CHAPS buffer, supplemented with 1 × protease inhibitors (Roche), and stored at −80°C. Upon thawing, samples were centrifuged at 12,000*g* for 10 min at 4°C, to remove debris, and then processed for western blot analysis.

Western blot analysis

Western blot analysis was performed according to standard methods. Total cell lysates in CHAPS buffer were quantified by BCA protein assay kit (Fisher Scientific #10678484) (except for co-IP samples) and denatured at 95°C for 5 min, prior to loading; 20–30µg of proteins were loaded per each lane on a 10% acrylamide—0.1% SDS gel. Afterwards, proteins were transferred to nitrocellulose membrane. Membranes were incubated 1 h in 1 × TBS-Tween containing 5% non-fat dry milk before to be exposed to primary antibodies at 4°C overnight. Then, membranes were washed three times in 1 × TBS-Tween, incubated 1 h with HRP-conjugated secondary antibodies (DAKO, 1:2000) in 1 × TBS-Tween containing 5% non-fat dry milk, at room temperature, washed again three times, and finally revealed by an ECL kit (GE Healthcare #GERPN2109). The following primary antibodies were used: anti-FOXG1, rabbit polyclonal, ChIP-grade, Abcam #ab18259, 1:1000 (Additional file 1: Fig. S1B); anti-FOXG1, rabbit polyclonal, a gift from G.Corte, 1:2000 (Additional file 1: Fig. S2B); anti-Flag, mouse monoclonal, clone M2, Sigma #F1804, 1:1000; anti-GRIN1-COOH-term, rabbit monoclonal, clone EPR2481(2), Abcam #ab109182, 1:5000; anti-beta-ACTIN, mouse monoclonal, HRP-conjugated, Sigma #A3854, 1:20000. Images were acquired by an Alliance LD2–77.WL apparatus (Uvitec, Cambridge) and analyzed by Uvitec Nine-Alliance software. Finally, protein levels were normalized against β-actin. Uncropped pictures of western blot assays are reported in Additional file 7: Fig. S6.

Numerical and statistical analysis

Full details of numerical and statistical analysis of data (including normalization criteria, number and definition of biological replicates, statistical tests employed for

result evaluation) are provided in the figures and their legends.

Full primary data referred to in Figs. 1, 2, 3, 4, 5, 6, 7, 8, 9, 10 and 11 and Additional file 1: Figures S1-5, as well as full details of their statistical evaluation, are reported in Additional file 8: Table S5.

Abbreviations

4OHT	4-Hydroxytamoxifen
aa	Amino acid
AMP	Adenosine monophosphate
APPRIS	Annotating principal splice isoforms software
ARC	Activity-regulated cytoskeleton-associated protein
ASD	Autism spectrum disorder
BCA	Bicinchoninic acid assay
BCD	Bicoid protein
Bdnf	Brain-derived neurotrophic factor
boi	Boundary of interest
Camk2b	Calcium/calmodulin-dependent protein kinase II beta
CASH	Comprehensive alternative splicing hunting software
cds	Coding sequence
CHAPS	3-((3-Cholamidopropyl) dimethylammonio)-1-propanesulfonate
COOH-term	Carboxy terminal
DeSeq2	Differentially expressed RNA Sequences software, version 2
DIV	Day in vitro
E	Embryonic day
EEF1D	Eukaryotic elongation factor 1D
EEF1G	Eukaryotic elongation factor 1G
EGFP	Enhanced green fluorescent protein
EIF4E	Eukaryotic initiation factor 4E
EIF4E-BP	EIF4E-binding protein
EIF4G	Eukaryotic initiation factor 4G
EMX2	Empty spiracles homeobox 2 protein
EN2	Engrailed homeobox 2 protein
ERT2	Estrogen receptor tamoxifen-binding domain, version 2
ex20	Exon 20
Flag	Flag epitope (DYKDDDDK)
Fmr1	Fragile X messenger ribonucleoprotein 1
FOXG1	Forkhead box G1 protein
Gabra1	Gamma-aminobutyric acid type A receptor subunit alpha1
GAD1	Glutamate decarboxylase 1
GO	Gene Ontology
Gria1	Glutamate ionotropic receptor AMPA type subunit 1
Grid1	Glutamate ionotropic receptor delta type subunit 1
Grin1	Glutamate ionotropic receptor NMDA type subunit 1
HOMER1	Homer scaffold protein 1
IF	Immunofluorescence
IP	Immunoprecipitated
iPSC	Induced pluripotent stem cell
LOF	Loss of function
LTP	Long-term potentiation
Mapt	MAPT-microtubule associated protein tau
MS	Mass spectrometry
mmu	Mus musculus
(n)	Nascent
NH2-term	Amino-terminal
NMDA	N-Methyl-D-aspartic acid
NMDAR	NMDA receptor
NMT1	N-Myristoyltransferase 1
NPAS4	Neuronal PAS domain protein 4
OE	Over-expressing
PLAP	Placental alkaline phosphatase (encoded by human ALPP gene)
PSD95	Postsynaptic density protein 95 (encoded by Dlg4 gene)
PUM1	Pumilio RNA-binding family member 1
puro-PLA	Puromycin proximity ligation assay
qRTPCR	Quantitative retrotranscription polymerase chain reaction
RiboDiff	Ribosomal (vs total) mRNA differential analysis software
RIP	RNA immunoprecipitation
rno	Rattus norvegicus
ROAR	Ratio of a ratio software
rpi	Ribosome progression index
Rpl10a	Ribosomal protein L10a
SGK1	Serum/glucocorticoid regulated kinase 1
SICER	Spatial clustering for identification of ChIP-enriched regions software
Slc17a6	Solute carrier family 17 member 6 (aka VGLUT2, vesicular glutamate transporter 2)
SMI312	Neurofilament medium chain antigen, recognized by the SMI312 antibody
SN	Supernatant
STAR	Spliced transcripts alignment to a reference software
TetON	Tetracycline-activated
totRNASeq	Total RNA reads
TRAP	Translating ribosome affinity purification
trapRNASeq	TRAP RNA reads
TSL	Transcript support level
TUBB3	Tubulin beta 3 class III
V5	V5 epitope (GKPIPNPLLGLDST)
WB	Western blot

Supplementary Information

The online version contains supplementary material available at https://doi.org/10.1186/s12915-024-01979-x.

Additional file 1: Figure S1. Evaluation of *Foxg1*-mRNA/FOXG1-protein expression levels in primary neocortical cultures, upon lentiviral delivery of a *Foxg1*-encoding or an anti-*Foxg1*-shRNA-encoding transgene. Figure S2. Assessment of FOXG1-protein interaction with selected translation factors in engineered HEK293T cells. Figure S3. Puro-PLA run off assay. Figure S4. Preliminary assesment of FOXG1-ERT2 confinement to cytoplasm. Figure S5. Validation of anti-FOXG1 antibodies employed in this study.

Additional file 2: Table S1. Levels of translation factor-encoding mRNAs in *Foxg1*-GOF neurons.

Additional file 3: Supplementary Results. Preliminary assesment of physical FOXG1 interaction with selected translation factors in engineered HEK293T cells

Additional file 4: Table S2A. List of genes with Foxg1-sensitive ribosome engagement. Table S2B. Genes with Foxg1-sensitive ribosome engagement: GO analysis. Table S2C. List of genes with Foxg1-sensitive ribosome progression index. Table S2D. Table S2D. Genes with Foxg1-sensitive ribosome progression index: GO analysis

Additional file 5: Table S3A. Index. Table S3B. totRNA: read counts and deseq analysis. Table S3C. trapRNA: read counts and deseq analysis. Table S3D. trapRNA and tot-RNA, deseq intersection and ribodiff analysis. Table S3E-H. trapRNA: read counts per bin, ctr 1-4. Table S3I-K. trapRNA: read counts per bin, f1oe 1-3. Table S3L. trapRNA: comparative analysis of reads distribution along cds', in ctr-vs-f1oe samples. Table S3M. ripRNA: analysis of Foxg1-protein/mRNA interaction islands

Additional file 6: Table S4. Plasmids and DNA fragments employed in this study: selected sequences

Additional file 7: Figure S6. Uncropped pictures of western blot assays reported in this study

Additional file 8: Table S5A. Index. Table S5B-K. Primary data and their statistical analysis, referring to Figures 1-9, and 11. Table S5L-N. Primary data and their statistical analysis, referring to Additional file 1: Figures S1-S3.

Acknowledgements

We thank Simone Mortal for helping us with preliminary hippocampal cell live-imaging tests.

We thank Cristina Fimiani for cloning "LVrc_TREt-pl-BGHpA", employed as the backbone of some lentiviruses used in this study, as well as Vittoria Avaro for helping with immunofluorescence controls.

We thank Sequentia (Barcelona, Spain) for the basic analysis of TRAPSeq and RIPSeq data as well as for splicing/polyA analysis of totRNASeq data.

Authors' contributions
O.A. performed experiments, analyzed data (including bioinformatic processing of tot-, trap- and rip-Seq data), and contributed to writing the manuscript. E.S.M. performed experiments and analyzed data, with particular emphasis on revision of the original manuscript. M.E. took care of bioinformatic analysis of tot-, trap-, and rip-Seq data. R.S. supervised bioinformatic analyses. A.M. designed the study, supervised its execution, prepared figures, wrote the manuscript, and revised them. All authors read and approved the final manuscript.

Funding
We thank the following:
(1) International FOXG1 Research Foundation (Grant to A.M.)
(2) Italian Ministery of University and Research (Grant PRIN22 2022M95RC7 to A.M.)
(3) SISSA (intramural funding to A.M. and YounGrant R_SSA-ALTR_YG_PS18_20_ NEUR_ref_gruppo_0517 to O.A.)

Availability of data and materials
All data generated or analyzed during this study are included in this published article, its supplementary information files, and publicly available repositories. In particular: (a) primary numerical values referred to by figure graphs are in Additional file 8_Table S5; (b) uncropped pictures of western blot assays reported in this study are in Additional file 7_Figure S6; and (c) raw totRNA, trapRNA, and ripRNA data employed for ribosome engagement and progression analyses [76] can be accessed at https://zenodo.org/records/13270734.

Declarations

Ethics approval and consent to participate
Animal handling and subsequent procedures were in accordance with European and Italian laws (European Parliament and Council Directive of 22 September 2010 (2010/63/EU); Italian Government Degree of 04 March 2014, no.26). Experimental protocols were approved by SISSA OpBA (Institutional SISSA Committee for Animal Care) and authorized by the Italian Ministery of Health (Auth. No 22DAB.N.4GU).

Consent for publication
Not applicable.

Competing interests
The authors declare that they have no competing interests.

Received: 4 August 2023 Accepted: 12 August 2024
Published online: 29 August 2024

References

1. Hanashima C, Fernandes M, Hebert JM, Fishell G. The role of Foxg1 and dorsal midline signaling in the generation of Cajal-Retzius subtypes. J Neurosci. 2007;27:11103–11.
2. Manuel M, Martynoga B, Yu T, West JD, Mason JO, Price DJ. The transcription factor Foxg1 regulates the competence of telencephalic cells to adopt subpallial fates in mice. Development. 2010;137:487–97.
3. Muzio L, Mallamaci A. Foxg1 confines Cajal-Retzius neuronogenesis and hippocampal morphogenesis to the dorsomedial pallium. J Neurosci. 2005;25:4435–41.
4. Martynoga B, Morrison H, Price DJ, Mason JO. Foxg1 is required for specification of ventral telencephalon and region-specific regulation of dorsal telencephalic precursor proliferation and apoptosis. Dev Biol. 2005;283:113–27.
5. Brancaccio M, Pivetta C, Granzotto M, Filippis C, Mallamaci A. Emx2 and Foxg1 inhibit gliogenesis and promote neuronogenesis. Stem Cells. 2010;28:1206–18.
6. Falcone C, Santo M, Liuzzi G, Cannizzaro N, Grudina C, Valencic E, et al. Foxg1 antagonizes neocortical stem cell progression to astrogenesis. Cereb Cortex. 2019;29:4903–18.
7. Frisari S, Santo M, Hosseini A, Manzati M, Giugliano M, Mallamaci A. Multidimensional functional profiling of human neuropathogenic FOXG1 alleles in primary cultures of murine pallial precursors. Int J Mol Sci. 2022;23:1343.
8. Santo M, Rigoldi L, Falcone C, Tuccillo M, Calabrese M, Martínez-Cerdeño V, et al. Spatial control of astrogenesis progression by cortical arealization genes. Cereb Cortex. 2023;33(6):3107–23.
9. Hanashima C, Li SC, Shen L, Lai E, Fishell G. Foxg1 suppresses early cortical cell fate. Science. 2004;303:56–9.
10. Miyoshi G, Fishell G. Dynamic FoxG1 expression coordinates the integration of multipolar pyramidal neuron precursors into the cortical plate. Neuron. 2012;74:1045–58.
11. Toma K, Kumamoto T, Hanashima C. The timing of upper-layer neurogenesis is conferred by sequential derepression and negative feedback from deep-layer neurons. J Neurosci. 2014;34:13259–76.
12. Hou P-S, Miyoshi G, Hanashima C. Sensory cortex wiring requires preselection of short- and long-range projection neurons through an Egr-Foxg1-COUP-TFI network. Nat Commun. 2019;10:3581.
13. Liu J, Yang M, Su M, Liu B, Zhou K, Sun C, et al. FOXG1 sequentially orchestrates subtype specification of postmitotic cortical projection neurons. Sci Adv. 2022;8:eabh3568.
14. Chiola S, Do MD, Centrone L, Mallamaci A. Foxg1 overexpression in neocortical pyramids stimulates dendrite elongation via Hes1 and pCreb1 upregulation. Cereb Cortex. 2019;29:1006–19.
15. Yu B, Liu J, Su M, Wang C, Chen H, Zhao C. Disruption of Foxg1 impairs neural plasticity leading to social and cognitive behavioral defects. Mol Brain. 2019;12:63.
16. Zhu W, Zhang B, Li M, Mo F, Mi T, Wu Y, et al. Precisely controlling endogenous protein dosage in hPSCs and derivatives to model FOXG1 syndrome. Nat Commun. 2019;10(1):928.
17. Tigani W, Rossi MP, Artimagnella O, Santo M, Rauti R, Sorbo T, et al. Foxg1 upregulation enhances neocortical activity. Cereb Cortex. 2020. https://doi.org/10.1093/cercor/bhaa107.
18. Artimagnella O, Mallamaci A. RNASeq profiling of Foxg1-GOF neocortical neurons. 2019. https://zenodo.org/records/2849657. Accessed 25 May 2019.
19. Fimiani C, Goina E, Su Q, Gao G, Mallamaci A. RNA activation of haploinsufficient Foxg1 gene in murine neocortex. Sci Rep. 2016;6:39311.
20. Shen L, Nam H-S, Song P, Moore H, Anderson SA. FoxG1 haploinsufficiency results in impaired neurogenesis in the postnatal hippocampus and contextual memory deficits. Hippocampus. 2006;16:875–90.
21. Miyoshi G, Ueta Y, Natsubori A, Hiraga K, Osaki H, Yagasaki Y, et al. FoxG1 regulates the formation of cortical GABAergic circuit during an early postnatal critical period resulting in autism spectrum disorder-like phenotypes. Nat Commun. 2021;12:3773.
22. Wong L-C, Singh S, Wang H-P, Hsu C-J, Hu S-C, Lee W-T. FOXG1-related syndrome: from clinical to molecular genetics and pathogenic mechanisms. IJMS. 2019;20:4176.
23. Brimble E, Reyes KG, Kuhathaas K, Devinsky O, Ruzhnikov MRZ, Ortiz-Gonzalez XR, et al. Expanding genotype–phenotype correlations in FOXG1 syndrome: results from a patient registry. Orphanet J Rare Dis. 2023;18:149.
24. ClinVar db_Foxg1. https://www.ncbi.nlm.nih.gov/clinvar/?term=Foxg1%5Bgene%5D. Accessed 6 Aug 2023.
25. SFARI db_Foxg1. https://gene.sfari.org/database/human-gene/Foxg1#variants-tab. Accessed 6 Aug 2023.
26. Florian C, Bahi-Buisson N, Bienvenu T. FOXG1-related disorders: from clinical description to molecular genetics. Mol Syndromol. 2011;2:153–63.

27. Mitter D, Pringsheim M, Kaulisch M, Plümacher KS, Schröder S, Warthemann R, et al. FOXG1 syndrome: genotype–phenotype association in 83 patients with FOXG1 variants. Genet Med. 2018;20:98–108.
28. Papandreou A, Schneider RB, Augustine EF, Ng J, Mankad K, Meyer E, et al. Delineation of the movement disorders associated with FOXG1 mutations: Table 1. Neurology. 2016;86:1794–800.
29. Vegas N, Cavallin M, Maillard C, Boddaert N, Toulouse J, Schaefer E, et al. Delineating FOXG1 syndrome: from congenital microcephaly to hyperkinetic encephalopathy. Neurol Genet. 2018;4:e281.
30. Mariani J, Coppola G, Zhang P, Abyzov A, Provini L, Tomasini L, et al. FOXG1-Dependent dysregulation of GABA/glutamate neuron differentiation in autism spectrum disorders. Cell. 2015;162:375–90.
31. Kumamoto T, Hanashima C. Evolutionary conservation and conversion of Foxg1 function in brain development. Dev Growth Differ. 2017;59:258–69.
32. Regad T, Roth M, Bredenkamp N, Illing N, Papalopulu N. The neural progenitor-specifying activity of FoxG1 is antagonistically regulated by CKI and FGF. Nat Cell Biol. 2007;9:531–40.
33. Pancrazi L, Di Benedetto G, Colombaioni L, Della Sala G, Testa G, Olimpico F, et al. Foxg1 localizes to mitochondria and coordinates cell differentiation and bioenergetics. Proc Natl Acad Sci USA. 2015;112:13910–5.
34. Li X, Wang W, Wang J, Malovannaya A, Xi Y, Li W, et al. Proteomic analyses reveal distinct chromatin-associated and soluble transcription factor complexes. Mol Syst Biol. 2015;11:775.
35. Stelzl U, Worm U, Lalowski M, Haenig C, Brembeck FH, Goehler H, et al. A human protein-protein interaction network: a resource for annotating the proteome. Cell. 2005;122:957–68.
36. Weise SC, Arumugam G, Villarreal A, Videm P, Heidrich S, Nebel N, et al. FOXG1 regulates PRKAR2B transcriptionally and posttranscriptionally via miR200 in the adult hippocampus. Mol Neurobiol. 2019;56:5188–201.
37. Nédélec S, Foucher I, Brunet I, Bouillot C, Prochiantz A, Trembleau A. Emx2 homeodomain transcription factor interacts with eukaryotic translation initiation factor 4E (eIF4E) in the axons of olfactory sensory neurons. Proc Natl Acad Sci USA. 2004;101:10815–20.
38. Baez MV, Cercato MC, Jerusalinsky DA. NMDA Receptor subunits change after synaptic plasticity induction and learning and memory acquisition. Neural Plast. 2018;2018:1–11.
39. Dörrbaum AR, Alvarez-Castelao B, Nassim-Assir B, Langer JD, Schuman EM. Proteome dynamics during homeostatic scaling in cultured neurons. eLife. 2020;9:e52939.
40. Zhou P, Zhang Y, Ma Q, Gu F, Day DS, He A, et al. Interrogating translational efficiency and lineage-specific transcriptomes using ribosome affinity purification. Proc Natl Acad Sci. 2013;110:15395–400.
41. Ingolia NT, Brar GA, Rouskin S, McGeachy AM, Weissman JS. The ribosome profiling strategy for monitoring translation in vivo by deep sequencing of ribosome-protected mRNA fragments. Nat Protoc. 2012;7:1534–50.
42. Argüello RJ, Reverendo M, Mendes A, Camosseto V, Torres AG, Ribas de Pouplana L, et al. SunRiSE—measuring translation elongation at single-cell resolution by means of flow cytometry. J Cell Sci. 2018;131:jcs214346.
43. Lau CG, Zukin RS. NMDA receptor trafficking in synaptic plasticity and neuropsychiatric disorders. Nat Rev Neurosci. 2007;8:413–26.
44. Paoletti P, Bellone C, Zhou Q. NMDA receptor subunit diversity: impact on receptor properties, synaptic plasticity and disease. Nat Rev Neurosci. 2013;14:383–400.
45. Rodriguez JM, Maietta P, Ezkurdia I, Pietrelli A, Wesselink J-J, Lopez G, et al. APPRIS: annotation of principal and alternative splice isoforms. Nucleic Acids Res. 2013;41 Database issue:D110–117.
46. Love MI, Huber W, Anders S. Moderated estimation of fold change and dispersion for RNA-seq data with DESeq2. Genome Biol. 2014;15:550.
47. Zhong Y, Karaletsos T, Drewe P, Sreedharan VT, Kuo D, Singh K, et al. RiboDiff: detecting changes of mRNA translation efficiency from ribosome footprints. Bioinformatics. 2017;33:139–41.
48. Wu W, Zong J, Wei N, Cheng J, Zhou X, Cheng Y, et al. CASH: a constructing comprehensive splice site method for detecting alternative splicing events. Brief Bioinform. 2018;19:905–17.
49. Grassi E, Mariella E, Lembo A, Molineris I, Provero P. Roar: detecting alternative polyadenylation with standard mRNA sequencing libraries. BMC Bioinformatics. 2016;17:423.
50. Feil R, Wagner J, Metzger D, Chambon P. Regulation of Cre recombinase activity by mutated estrogen receptor ligand-binding domains. Biochem Biophys Res Commun. 1997;237:752–7.
51. Whitfield J, Littlewood T, Evan GI, Soucek L. The estrogen receptor fusion system in mouse models: a reversible switch. Cold Spring Harb Protoc. 2015;2015:227–34.
52. Ainsley JA, Drane L, Jacobs J, Kittelberger KA, Reijmers LG. Functionally diverse dendritic mRNAs rapidly associate with ribosomes following a novel experience. Nat Commun. 2014;5:4510.
53. Cajigas IJ, Tushev G, Will TJ, tom Dieck S, Fuerst N, Schuman EM. The local transcriptome in the synaptic neuropil revealed by deep sequencing and high-resolution imaging. Neuron. 2012;74:453–66.
54. Kügelgen N, Chekulaeva M. Conservation of a core neurite transcriptome across neuronal types and species. WIREs RNA. 2020;11(4):e1590.
55. Middleton SA, Eberwine J, Kim J. Comprehensive catalog of dendritically localized mRNA isoforms from sub-cellular sequencing of single mouse neurons. BMC Biol. 2019;17:5.
56. Liuzzi G, Artimagnella O, Frisari S, Mallamaci A. Foxg1 bimodally tunes L1-mRNA and -DNA dynamics in the developing murine neocortex. Development. 2024;151:dev202292.
57. Jackson RJ, Hellen CUT, Pestova TV. The mechanism of eukaryotic translation initiation and principles of its regulation. Nat Rev Mol Cell Biol. 2010;11:113–27.
58. Pelletier J, Sonenberg N. The organizing principles of eukaryotic ribosome recruitment. Annu Rev Biochem. 2019;88:307–35.
59. Srivastava T, Fortin DA, Nygaard S, Kaech S, Sonenberg N, Edelman AM, et al. Regulation of neuronal mRNA translation by CaM-Kinase I phosphorylation of eIF4GII. J Neurosci. 2012;32:5620–30.
60. Niessing D, Blanke S, Jäckle H. Bicoid associates with the 5′-cap-bound complex of caudal mRNA and represses translation. Genes Dev. 2002;16:2576–82.
61. Brunet I, Weinl C, Piper M, Trembleau A, Volovitch M, Harris W, et al. The transcription factor Engrailed-2 guides retinal axons. Nature. 2005;438:94–8.
62. Ingolia NT, Ghaemmaghami S, Newman JRS, Weissman JS. Genome-wide analysis in vivo of translation with nucleotide resolution using ribosome profiling. Science. 2009;324:218–23.
63. Brigidi GS, Hayes MGB, Delos Santos NP, Hartzell AL, Texari L, Lin P-A, et al. Genomic decoding of neuronal depolarization by stimulus-specific NPAS4 heterodimers. Cell. 2019;179:373–391.e27.
64. Steward O, Matsudaira Yee K, Farris S, Pirbhoy PS, Worley P, Okamura K, et al. Delayed degradation and impaired dendritic delivery of intron-lacking EGFP-Arc/Arg3.1 mRNA in EGFP-Arc transgenic mice. Front Mol Neurosci. 2018;10:435.
65. Tucker KL, Meyer M, Barde YA. Neurotrophins are required for nerve growth during development. Nat Neurosci. 2001;4:29–37.
66. Spigoni G, Gedressi C, Mallamaci A. Regulation of Emx2 expression by antisense transcripts in murine cortico-cerebral precursors. PLoS One. 2010;5:e8658.
67. Raciti M, Granzotto M, Duc MD, Fimiani C, Cellot G, Cherubini E, et al. Reprogramming fibroblasts to neural-precursor-like cells by structured overexpression of pallial patterning genes. Mol Cell Neurosci. 2013;57:42–53.
68. Tom Dieck S, Kochen L, Hanus C, Heumüller M, Bartnik I, Nassim-Assir B, et al. Direct visualization of newly synthesized target proteins in situ. Nat Methods. 2015;12:411–4.
69. Heiman M, Kulicke R, Fenster RJ, Greengard P, Heintz N. Cell type-specific mRNA purification by translating ribosome affinity purification (TRAP). Nat Protoc. 2014;9:1282–91.
70. Zhou L, Lim Q-E, Wan G, Too H-P. Normalization with genes encoding ribosomal proteins but not GAPDH provides an accurate quantification of gene expressions in neuronal differentiation of PC12 cells. BMC Genomics. 2010;11:75.
71. Kinsella RJ, Kahari A, Haider S, Zamora J, Proctor G, Spudich G, et al. Ensembl BioMarts: a hub for data retrieval across taxonomic space. Database. 2011;2011:bar030.
72. Langmead B, Salzberg SL. Fast gapped-read alignment with Bowtie 2. Nat Methods. 2012;9:357–9.
73. Liao Y, Smyth GK, Shi W. featureCounts: an efficient general purpose program for assigning sequence reads to genomic features. Bioinformatics. 2014;30:923–30.

74. Kolberg L, Raudvere U, Kuzmin I, Vilo J, Peterson H. gprofiler2 – an R package for gene list functional enrichment analysis and namespace conversion toolset g:Profiler. F1000Res. 2020;9:709.
75. Xu S, Grullon S, Ge K, Peng W. Spatial clustering for identification of ChIP-enriched regions (SICER) to map regions of histone methylation patterns in embryonic stem cells. In: Kidder BL, editor. Stem cell transcriptional networks. New York: Springer, New York; 2014. p. 97–111.
76. Mallamaci A, Artimagnella O. Foxg1 regulation of translation: RNASeq data. 2024. https://zenodo.org/records/13270734. Accessed 8 Aug 2024.

Publisher's Note